☙

First-principles theory of field-effect doping in transition-metal dichalcogenides: Structural properties, electronic structure, Hall coefficient, and electrical conductivity

Thomas Brumme,[*] Matteo Calandra, and Francesco Mauri

CNRS, UMR 7590 and Sorbonne Universités, UPMC Univ Paris 06, IMPMC - Institut de Minéralogie, de Physique des Matériaux,
et de Cosmochimie, 4 place Jussieu, F-75005 Paris, France

We investigate how field-effect doping affects the structural properties, the electronic structure, and the Hall coefficient of few-layers transition-metal dichalcogenides by using density-functional theory. We consider monolayers, bilayers, and trilayers of the H polytype of MoS_2, $MoSe_2$, $MoTe_2$, WS_2, and WSe_2 and provide a full database of electronic structures and Hall coefficients for hole and electron doping. We find that, for both electron and hole doping, the electronic structure depends on the number of layers and cannot be described by a rigid band shift. Furthermore, it is important to relax the structure under the asymmetric electric field. Interestingly, while the width of the conducting channel depends on the doping, the number of occupied bands at each given $\mathbf{k}$ point is almost uncorrelated with the thickness of the doping-charge distribution. Finally, we calculate within the constant-relaxation-time approximation the electrical conductivity and the inverse Hall coefficient. We demonstrate that in some cases the charge determined by Hall-effect measurements can deviate from the real charge by up to 50%. For hole-doped $MoTe_2$ the Hall charge has even the wrong polarity at low temperature. We provide the mapping between the doping charge and the Hall coefficient. We present more than 250 band structures for all doping levels of the transition-metal dichalcogenides considered within this work.

I. INTRODUCTION

Since the rise of graphene [1] and the discovery of topological insulators [2] a lot of interesting physics has been found in systems with reduced dimensions. Other two-dimensional (2D) material, such as monolayers or few-layer systems (nanolayers) of transition-metal dichalcogenides [3–7] (TMDs) are gaining importance because of their intrinsic band gap. TMDs are MX_2-type compounds where M is a transition metal (e.g., $M =$ Mo, W) and X represents a chalcogen (S, Se, Te). These materials form layered structures in which the different X-M-X layers are held together by weak van der Waals forces. Thus, similar to graphene, one can easily extract single or few layers from the bulk compound using the mechanical-exfoliation or other experimental techniques.

Doping these nanolayers with field-effect transistors (FETs) is particularly appealing [8–21] as it allows for the exploration of the semiconducting, metallic, superconducting, and charge-density-wave regimes in reduced dimensionality. Furthermore, the TMDs are promising materials to realize valleytronics, i.e., the usage of the valley index of carriers to process information [7,15,22].

Despite these challenging experimental perspectives, the understanding of structural, electronic, and transport properties at high electric field in FET configuration is still limited, particularly in the physically relevant case of multilayer samples. Previous theoretical works [20,23] analyzed the high doping limit of 20 nm thick MoS_2 flakes [10], relevant for ionic-liquid-based FETs, by assuming that only the topmost layer is doped uniformly. However, it is unclear to what extent the doping of thick flakes can be modeled in this approximation as the thickness of the conductive channel is not experimentally accessible.

A second crucial issue is the determination of the doping charge. Usually the charge is determined via Hall-effect measurements. However, the interpretation of Hall experiments assumes a 2D electron-gas model, most likely valid only in the low doping regime. In TMDs, due to the multivalley electronic structure, this assumption is highly questionable.

In this paper we solve these issues and provide a thorough study of structural, electronic, and transport properties and of their changes under field-effect doping for TMDs. We use our recently developed first-principles theoretical approach to model doping in field-effect devices [24]. The method allows for calculation of the electronic structure as well as complete structural relaxation in field-effect configuration using density-functional theory (DFT). We apply our approach to the H polytype of MoS_2, $MoSe_2$, $MoTe_2$, WS_2, and WSe_2.

The paper is organized as follows: In Sec. II we summarize the parameters and methods used within the paper and the relaxed geometries of the bulk TMDs. Then we will first show the results for the undoped monolayer, bilayer, and trilayer systems (Sec. III A). After a brief discussion on the quantum capacitance (Sec. III B), we will investigate the changes of the geometry and the electronic structure of the different TMDs in Secs. III C and III D, respectively. Finally, we will focus on how the doping-charge concentration can be determined experimentally by Hall-effect measurements. We will show in Sec. III E that the results of such a measurement cannot be interpreted within a 2D electron-gas model but that the specific band structure of the TMDs and its changes in a field-effect setup need to be taken into account. In Sec. III F we will furthermore investigate the density of states (DOS) at the Fermi energy and the electrical conductivity as a function of doping. In the end, we will summarize our results and draw some final conclusion in Sec. IV. In the Supplemental Material [25] we provide a full database of electronic structures for all doping levels considered in this work (in total more

---

*thomas.brumme@impmc.upmc.fr

TABLE I. Comparison of the calculated and experimental [31] lattice parameters.

	a calc.	a exp.	c calc.	c exp.
MoS_2	3.197 Å	3.160 Å	12.38 Å	12.29 Å
$MoSe_2$	3.328 Å	3.289 Å	13.07 Å	12.93 Å
$MoTe_2$	3.536 Å	3.518 Å	14.00 Å	13.97 Å
WS_2	3.190 Å	3.153 Å	12.15 Å	12.32 Å
WSe_2	3.341 Å	3.282 Å	12.87 Å	12.96 Å

than 250 calculations, Figs. S10–S45) and Hall coefficients (Figs. S46–S48) of monolayer, bilayer, and trilayer dichalcogenides as a function of doping.

II. COMPUTATIONAL DETAILS

All calculations were performed within the framework of DFT using the QUANTUM ESPRESSO package [26], which uses a plane-wave basis set to describe the valence-electron wave function and charge density. We employed full-relativistic, projector-augmented wave potentials [27]. While the local-density approximation is known to underestimate the lattice parameters, generalized-gradient approximations for the exchange-correlation energy overestimate the out-of-plane lattice constant (see, e.g., Ref. [28] and references therein). In our FET setup a correct description of the interlayer distance is, however, very important. Accordingly, we choose the Perdew-Burke-Ernzerhof functional [29] (PBE) for the exchange-correlation energy and furthermore included dispersion corrections [30] (D2). This also leads to the best agreement with both the experimental in-plane and out-of-plane lattice parameters (cf. Table I). A comparison between PBE and LDA for MoS_2 can be found in the Supplemental Material (Fig. S9).

Using the experimental lattice parameters of the H polytype of the bulk structures [31] as starting geometry, we minimized the total energy as a function of the lattice parameters until it changed by less then 2 meV. For the molybdenum-containing dichalcogenides we used a cutoff of 50 Ry and 410 Ry (1 Ry ≈ 13.6 eV) for the wave functions and the charge density, respectively, while for the tungsten dichalcogenides we chose 55 Ry/410 Ry. The Brillouin zone (BZ) integration has been performed with a Monkhorst-Pack grid [32] of $16 \times 16 \times 4$ **k** points and using a Gaussian broadening of 0.002 Ry ≈ 27 meV. The convergence with respect to the number of **k** points as well as the wave-function and charge-density cutoff has been checked. The self-consistent solution of the Kohn-Sham equations was obtained when the total energy changed by less than 10^{-9} Ry and the maximum force on all atoms was less than 5×10^{-4} Ry a_0^{-1} ($a_0 \approx 0.529177$ Å is the Bohr radius). The lattice parameters thus determined are given in Table I and agree within 2% with the experimental values.

The final geometry of the bulk system was used as the starting geometry for the relaxation of the layered 2D systems in an FET setup. To achieve this, the size of the unit cell was fixed in plane and the perpendicular size was increased such that the vacuum region between the repeated images was at least 23 Å. The layers were stacked as in the H polytype of the bulk compound. The BZ integration has been performed with a

TABLE II. Conversion for the doping-charge concentration n (in e/unit cell) to charge-carrier concentration n per area cm^{-2} for the different dichalcogenides and two typical doping-charge concentrations of n = 0.01 e/unit cell and n = 0.15 e/unit cell.

	n = 0.01 e/unit cell	n = 0.15 e/unit cell
MoS_2	$n \approx 0.1127 \times 10^{14}$ cm^{-2}	$n \approx 1.6911 \times 10^{14}$ cm^{-2}
$MoSe_2$	$n \approx 0.1042 \times 10^{14}$ cm^{-2}	$n \approx 1.5636 \times 10^{14}$ cm^{-2}
$MoTe_2$	$n \approx 0.0924 \times 10^{14}$ cm^{-2}	$n \approx 1.3856 \times 10^{14}$ cm^{-2}
WS_2	$n \approx 0.1135 \times 10^{14}$ cm^{-2}	$n \approx 1.7027 \times 10^{14}$ cm^{-2}
WSe_2	$n \approx 0.1035 \times 10^{14}$ cm^{-2}	$n \approx 1.5521 \times 10^{14}$ cm^{-2}

Monkhorst-Pack grid of $64 \times 64 \times 1$ **k** points for the charged systems and $16 \times 16 \times 1$ **k** points for the neutral ones. In order to correctly determine the Fermi energy in the charged systems, we performed a non-self-consistent calculation on a denser **k**-point grid of at least $90 \times 90 \times 1$ points starting from the converged charge density. All other parameters were the same as in the calculations for the bulk systems. For the total-energy calculations of the 1T and 1T' polytype of MoS_2 and WSe_2 under FET doping, we doubled the unit-cell size along one in-plane direction and correspondingly halved the number of **k** points along this direction.

Several methods have been developed to study electrostatics in periodic boundary condition [24,33–35] with different experimental geometries. We used our recently developed method [24] as it is tailored for the FET setup and allows for structural optimization. The dipole for the dipole correction [24,36] was placed at $z_{dip} = d_{dip}/2$ with $d_{dip} = 0.01 L$ and L being the unit-cell size in the direction perpendicular to the 2D plane—L changed for the different calculations and was between 34 Å and 48 Å. The charged plane modeling the gate electrode [24] was placed close to the dipole at $z_{mono} = 0.011 L$. A potential barrier with a height of $V_0 = 2.5$ Ry and a width of $d_b = 0.1 L$ was used in order to prevent the ions from moving too close to the gate electrode. The final results were found to be independent of the separation of the dipole planes, as well as the barrier height and width as long as it is high or thick enough to ensure that the electron density at the position of the dipole and the gate electrode is zero, $\rho^e(z_{mono}) = \rho^e(z_{dip}) = 0$. As we will often give the doping-charge concentration per unit cell n (i.e., in charge per unit cell, e/unit cell, with the elementary charge $e \approx 1.602 \times 10^{-19}$ C), we summarized in Table II the conversion to charge-carrier concentration per area n (in cm^{-2}) for the different dichalcogenides and two typical doping-charge concentrations of n = 0.01 e/unit cell and n = 0.15 e/unit cell. Throughout the paper we will use $n < 0$ and $n > 0$ for electron and hole doping, respectively. Typical charge-carrier concentrations, which can be achieved in experiments using either solid-state dielectrics such as SiO_2 or ionic-liquid-based FETs, can be found in Table III. Note that in principle those maximum concentrations could be possible for all TMDs [37] even if we did not find references for, e.g., ionic-liquid-based field-effect doping of $MoSe_2$.

In order to calculate the Hall tensor $R_{ijk}(T; E_F)$, we used the BOLTZTRAP code [45] to determine the conductivity tensors in Eqs. (11) and (12) (see Sec. III E for more details).

TABLE III. Maximum experimental charge-carrier concentration n per area cm^{-2} for the different dichalcogenides using either a solid-state or an ionic-liquid-based FET. References are given after the charge-carrier concentration.

	Polarity	Solid-state FET	Ionic-liquid FET
MoS$_2$	n-type	$\approx -3.6 \times 10^{13}$ [14]	$\approx -9.8 \times 10^{14}$ [38]
	p-type	–	–
MoSe$_2$	n-type	$\approx -3.9 \times 10^{12}$ [39]	–
	p-type	$\approx +2.0 \times 10^{12}$ [39]	–
MoTe$_2$	n-type	$\approx -1.3 \times 10^{13}$ [40]	$\approx -1.1 \times 10^{13}$ [41]
	p-type	–	$\approx +1.8 \times 10^{13}$ [41]
WS$_2$	n-type	$\approx -1.0 \times 10^{14}$ [19]	$\approx -4.0 \times 10^{14}$ [42]
	p-type	–	$\approx +3.5 \times 10^{13}$ [43]
WSe$_2$	n-type	–	$\approx -1.4 \times 10^{14}$ [16]
	p-type	$\approx +9.0 \times 10^{12}$ [44]	$\approx +1.9 \times 10^{15}$ [16]

We fitted the band structure for each doping of the different TMDs by using 55 times more plane waves than bands and used afterwards the in-plane components of the energy-projected tensors to calculate the Hall coefficient $R_{xyz}(T; E_F)$ for temperature T and chemical potential E_F. $R_{xyz}(T; E_F)$ is the only relevant Hall coefficient for our 2D systems assuming that the magnetic field is applied perpendicular to the layers. We checked the convergence by calculating $R_{xyz}(T; E_F)$ with increasing number of **k** points and found that the results for the $64 \times 64 \times 1$ grid and the dense grid of the non-self-consistent calculation are the same.

III. RESULTS

A. Electronic structure of TMDs

In the following we will first briefly summarize the results for the undoped TMDs before investigating the changes under field-effect doping. We focus on the changes in the valence-band maximum and the conduction-band minimum with changing transition metal or chalcogen and compare them with other results found in literature [28].

Figure 1 shows the band structure and the projected density of states (pDOS) for monolayer MoSe$_2$ with and without including spin-orbit coupling (SOC). Monolayer molybdenum diselenide is (as most TMDs) a direct-band-gap semiconductor with a DFT gap of about 1.329 eV at the K point. Our calculated gap is smaller by 83 meV than the one in Ref. [28], which can be attributed to our slightly larger in-plane lattice parameter as the size of the band gap decreases with increasing lattice constant [46–49]. This is due to the fact that the valence-band maximum at K is formed by in-plane states of both the transition metal and the chalcogen [49]. On the other hand, the conduction-band minimum at K is mainly formed by out-of-plane Mo states (d_{z^2} without SOC and $m_j = \pm 1/2$ for both $j = 5/2$ and $j = 3/2$ including SOC) and in-plane states of the chalcogen. The valence-band maximum near Γ has basically only out-of-plane states of Mo and Se as can be seen in Fig. 1. This will become very important for hole doping of the nanolayers in an FET setup—depending on which valley is doped (K or Γ) one can expect different doping-charge distributions. Energetically very close to the conduction-band minimum at K is a minimum halfway between K and Γ.
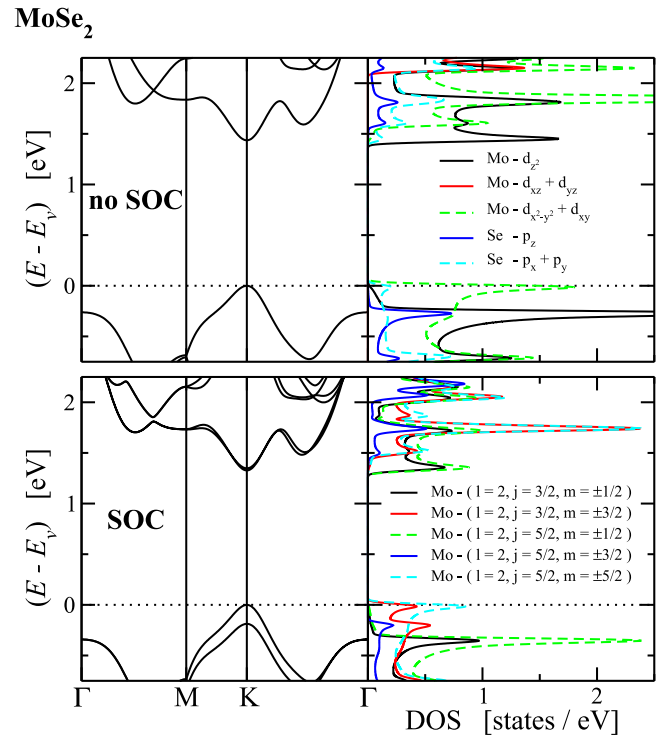
MoSe$_2$

FIG. 1. (Color online) Band structure and density of states projected onto atomic orbitals for monolayer MoSe$_2$ without (top) and with (bottom) including spin-orbit coupling. The energy is given relative to the valence-band maximum E_v. As apparent in the case without SOC, mainly in-plane states contribute to the valence-band maximum near K (Mo $d_{x^2-y^2}$ and d_{xy}, Se $p_{x/y}$), while the maximum near Γ is formed by out-of-plane states (Mo d_{z^2}, Se p_z). This also holds in the SOC case where the valence-band states with mainly in-plane character can be found near K ($j = 5/2, m_j = \pm 5/2, \pm 3/2$ and $j = 3/2, m_j = \pm 3/2$) while those with more out-of-plane character can be found near Γ ($m_j = \pm 1/2$ for both $j = 5/2$ and $j = 3/2$, see Ref. [51] for the states in terms of spherical harmonics). On the other hand, the conduction-band minimum near K has mainly contributions from out-of-plane Mo and in-plane Se states (without SOC: Mo d_{z^2} and Se $p_{x/y}$, with SOC: Mo $m_j = \pm 1/2$ for both $j = 5/2$ and $j = 3/2$).

The corresponding point in **k** space is called Q in literature (sometimes Λ or $\Lambda_{\min}$ as it is a minimum along the Λ line, from Γ to K) even if it is not a high symmetry point of the BZ. This is also why this minimum does not lie exactly at the same point for the different TMDs and its position can even change if the number of layers is increased. The states close to the Q point have a stronger in-plane character and can thus also lead to a different doping-charge distribution if the doping occurs mainly at this point in the BZ. The same results for the character of the different valleys were also obtained in Refs. [48–50].

The different character of the states in the different valleys is even more important for the other TMDs. From sulfur to tellurium the difference between the minimum at K and Q decreases: for MoS$_2$ the minimum at K is lower by 279 meV while it is only 154 meV and 72 meV lower for MoSe$_2$ and MoTe$_2$, respectively. The change in the case of the tungsten dichalcogenides is much lower, which, however, might be
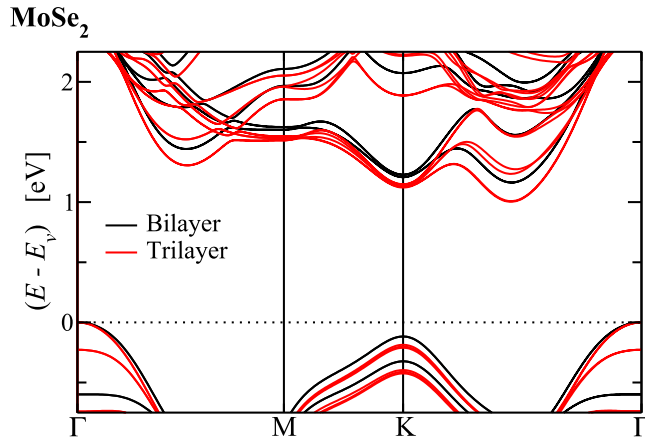
MoSe$_2$

FIG. 2. (Color online) Band structure for bilayer and trilayer MoSe$_2$. The energy is given relative to the valence-band maximum E_v. Molybdenum diselenide changes (as all TMDs investigated in this paper) from a direct-band-gap semiconductor to an indirect one when the number of layers is increased.
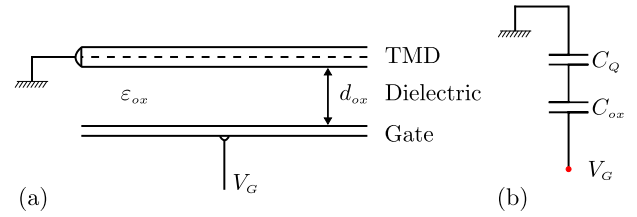

FIG. 3. (Color online) (a) Schematic illustration of an FET setup in which the 2D metallic system is separated from the gate electrode by a dielectric with dielectric constant ε_{ox} of thickness d_{ox}. (b) Equivalent circuit for the overall capacitance seen at the gate electrode.

due to the stronger spin-orbit splitting of the bands near Q compared the splitting at K. The band structures of all undoped TMDs are summarized in the Supplemental Material [25], Figs. S1–S5.

Increasing the number of layers in TMDs leads to a well-known change from a direct-band-gap semiconductor to an indirect one [28,50,52–55] as shown in Fig. 2. The change of the direct band gap at K with increasing the number of layers is much smaller than the changes at Γ or Q. This is due to the small hybridization between different layers at K as those states have only in-plane chalcogen character. On the other hand, both valleys at Γ and Q have contributions from Se p_z states. Accordingly, the maximum (minimum) at Γ (Q) shift up (down) in energy, which eventually leads to an indirect band gap between Γ and Q (see also Ref. [50] for an in-depth analysis). The transition between the indirect gap $\Gamma \rightarrow K$ and $\Gamma \rightarrow Q$ happens at different number of layers and occurs either in the bilayer case (MoSe$_2$), in the trilayer case (WS$_2$ and WSe$_2$), or in the bulk limit (MoS$_2$, MoTe$_2$). Depending on the level of theory that was used, one can also find very different results in literature when this transition occurs. Most calculations were done for MoS$_2$ for which the transition either already occurs for the bilayer [47,56,57] or with larger number of layers [58–60]. In fact, Ramasubramaniam *et al.* have shown in Ref. [61] that using the experimental bulk distance between the layers in the bilayer case also leads to an indirect band gap $\Gamma \rightarrow Q$ while relaxation using PBE+D2 leads to an indirect gap $\Gamma \rightarrow K$. Also for other TMDs one can find different results [47,60,62–64]. For a comprehensive review of the theoretical papers see also Ref. [28] and references therein. Molybdenum ditelluride is especially peculiar, since the calculations show that its valence-band maximum is located at K even in the trilayer case. Furthermore, we find that the difference between the maximum at Γ and K is only 26 meV in bulk MoTe$_2$ which is in agreement with the experimental results in Ref. [65].

In Sec. III D we will see that, e.g., the varying difference between the conduction-band minimum at K and Q for the

different TMDs will also lead to a different thickness of the conductive channel for electron doping in an FET setup, while nearly all TMDs will behave similarly under hole doping. However, before investigating the changes under field-effect doping we want to focus on another problem that can make it difficult to dope a 2D system—the quantum capacitance.

B. Quantum capacitance

A prominent example in which the quantum capacitance hinders the doping via field-effect setup is graphene. Due to its linear dispersion relation at the K points, the charge that can be induced in an FET setup is much smaller than the corresponding charge at the gate electrode [66,67]. Thus, doping concentrations exceeding 10^{13} cm^{-2} are hardly achievable using common dieletrics such as SiO$_2$ or HfO$_2$. Similarly, the quantum capacitance in nanolayers of TMDs could also reduce the amount of induced charge. In the following we want to show that TMDs are, however, quite different from graphene and that the quantum capacitance is not relevant in their case as soon as the Fermi energy is within the conduction or valence band. In fact, experimentally doping concentrations in the order of 10^{14} cm^{-2} are possible using ionic-liquid-based FETs [10,16,42,68,69] (cf. Table III).

The term "quantum capacitance" was first used by Luryi [70] in order to develop an equivalent circuit model to describe the incomplete screening of an electric field by a 2D electron gas. When a 2D metallic system is contacted by a gate electrode [separated by a dielectric as shown in Fig. 3(a)], the electric field generated by the charges on the dielectric surface leads to a shift of the Fermi level of the 2D metal. This effect results in a modified capacitance with respect to the geometrical capacitance C_{ox} per unit surface

$$C_{ox} = \varepsilon_{ox} \varepsilon_0 \, d_{ox}^{-1}, \tag{1}$$

obtained for a capacitor having a dielectric constant ε_{ox} and thickness d_{ox}.

As shown in Fig. 3(b), the quantum capacitance C_Q is in series with that of the dielectric, namely

$$\frac{1}{C} = \frac{1}{C_{ox}} + \frac{1}{C_Q}. \tag{2}$$

Under the simplified assumption that both C_{ox} and C_Q are independent of the applied gate voltage V_G, the charge induced

TABLE IV. Geometrical capacitances for parallel-plate capacitors with 100 nm SiO_2 (relative permittivity $\varepsilon_r = 3.9$), 10 nm HfO_2 ($\varepsilon_r \approx 20$), and an 1 nm thick ionic-liquid (IL) FET ($\varepsilon_r \approx 15$), quantum capacitance for electron doping of the K valley ($m \approx 0.5m_0$) and hole doping of the Γ valley ($m \approx m_0$) of MoS_2 ($\nu = 4$), and the overall capacitance of a setup as shown in Fig. 3(b). All capacitances are given in units of $\mu F\,cm^{-2}$.

	$C_Q^K = 133.9$	$C_Q^\Gamma = 267.7$
$C_{SiO_2} = 0.035$	$C = 0.035$	$C = 0.035$
$C_{HfO_2} = 1.771$	$C = 1.748$	$C = 1.759$
$C_{IL} = 13.28$	$C = 12.08$	$C = 12.65$

in the 2D system n_Q can be written as:

$$
n_Q = \begin{cases} 0 & \forall\, V_G \in (V_v, V_c) \\ C(V_v - V_G) & \forall\, V_G < V_v \\ C(V_c - V_G) & \forall\, V_G > V_c \end{cases}, \quad (3)
$$

where V_v and V_c are the onset potentials to fill the valence-band minimum or conduction-band maximum, respectively. Thus, when $C_Q \gg C_{ox}$, we have

$$
C = C_{ox}\left(1 + \frac{C_{ox}}{C_Q}\right)^{-1} \approx C_{ox} \quad (4)
$$

and we regain the classical result, i.e., the charge that can be induced in the 2D system depends only on the applied gate voltage and the capacitance between gate and sample.

As shown in Refs. [70,71], the quantum capacitance in this case and for gate voltages larger (smaller) than the onset potential of the conduction band (valence band) is given by

$$
C_Q = \frac{g_s g_v m q^2}{\pi \hbar^2}, \quad (5)
$$

where g_s and g_v, m, and q are the spin and valley degeneracies, the effective mass, and the charge, respectively. Depending on (i) the dielectric thickness d_{ox}, (ii) the effective mass of the 2D metallic system, and (iii) the number of valleys $\nu = g_s g_v$, the quantum capacitance C_Q can be relevant or not.

Table IV shows the total capacitance, geometrical capacitance for typical gate dielectrics, and the quantum capacitance for electron doping of the K valley or hole doping of the Γ valley of MoS_2 (the effective masses of the different valleys were taken from Ref. [47]). As the geometrical capacitance of a parallel-plate capacitor increases with decreasing thickness of the dielectric, an ionic-liquid (IL) FET with an 1 nm thick electric double layer (inner Helmholtz plane) shows the largest deviation of the total capacitance C from the geometrical capacitance C_{IL}—even for a thin dielectric layer of 10 nm HfO_2, $C \approx 0.986\, C_{HfO_2}$. Yet, for TMDs the number of valleys increases with increasing doping (valleys at K and Q or K and Γ for electron or hole doping, respectively), which also leads to a considerably larger DOS at the Fermi energy than for a single quadratic band. Thus, the quantum capacitance C_Q is further increased [71], which in turn leads to $C \approx C_{ox}$. Similar results have been found by Ma and Jena in Ref. [72] who also provide a detailed description of the low-doping regime $n < 10^{13}\,cm^{-2}$

C. Structural changes under field-effect doping

The doping via FET setup has only a minor influence on the structure of the TMDs—the changes are much smaller than for, e.g., ZrNCl [24]. This is due to the weak polarity of the bond between the transition-metal and the chalcogen. The largest change can be found for the layer thickness (z component of the chalcogen-chalcogen vector) of the layer closest to the charged plane representing the gate electrode—the layer thickness increases by ≈ 0.06 Å for a large electron doping of $n = -0.3\,e$/unit cell ($n \approx -3.16 \times 10^{14}\,cm^{-2}$) and decreases by ≈ 0.02 Å for a large hole doping of $n = +0.3\,e$/unit cell. This change is mainly due to the increase/decrease of the chalcogen–transition-metal bond length of those being closest to the gate—we find $\approx +0.04$ Å for $n = -0.3\,e$/unit cell and ≈ -0.02 Å for $n = +0.3\,e$/unit cell. Accordingly, there is also a small change in the angle between the first chalcogen, the transition-metal, and the second chalcogen of up to $+0.9°$ ($-0.4°$) for large electron (hole) doping. Note that even if the structural changes seem to be small it is still important to relax the system in the FET setup. Otherwise, the band structure can be quite different for doping $|n| > 0.15\,e$/unit cell as exemplified in Fig. S6 in the Supplemental Material [25].

Even if the internal structure changes only slightly under FET doping, electron doping could induce a phase transition where the structure of the full nanolayer system is altered. It is well known that lithium [73,74] or potassium [75] intercalated MoS_2 can undergo a phase transition in which the Mo coordination changes from a direct-band-gap, semiconducting, trigonal-prismatic structure (labeled 2H, "2" as there are two layers in the unit cell) to a metallic, octahedral one (1T). It has been found experimentally [76,77] and shown theoretically [78,79], that also monolayer MoS_2 can undergo this phase transition. In the calculations, for a high electron doping by H (Ref. [78]) or Li (Ref. [79]) adsorption of $n \approx -0.35\,e$/unit cell or $n = -0.44\,e$/unit cell, respectively, the octahedral phases such as the 1T or 1T$'$ phases become more stable than the 1H phase. In the 1T$'$ phase the molybdenum forms zigzag chains like tungsten in WTe_2 [80–85]. Such a transition was also found experimentally by rhenium doping of WS_2 nanotubes [86] and monolayer MoS_2 [87], and by transfer of hot electrons generated in gold nanoparticles to monolayer MoS_2 [88]. In order to determine if the FET setup can lead to such a phase transition for electron doping, we compare in Fig. 4 the total energy for the monolayer structures of 1T-MoS_2 and 1T$'$-MoS_2 ($E_{x\text{-}MoS_2}^{tot}$) with the total energy of the 1H polytype ($E_{1H\text{-}MoS_2}^{tot}$). We find that the 1T$'$ structure becomes more stable for electron doping larger than $n = -0.44\,e$/unit cell in close agreement with the results of Refs. [78,79]. Thus, it seems that the interaction between the H/Li atoms and the MoS_2 layer has only a minor influence on the phase stability as the transition occurs in our FET setup at the same doping. We also calculated the energy difference between 1T$'$-WSe_2 and 1H-WSe_2, ($E_{1T'\text{-}WSe_2}^{tot} - E_{1H\text{-}WSe_2}^{tot}$), for a few concentrations of electron doping and found that for a concentration of $n = -0.35\,e$/unit cell the 1T$'$ polytype becomes more stable by 63 meV. In the following, we will thus only consider doping of the H polytype with electron concentrations $n \geqslant -0.35\,e$/unit cell as it is the most stable structure found in nature and is often used to prepare the samples by the mechanical-cleavage method.
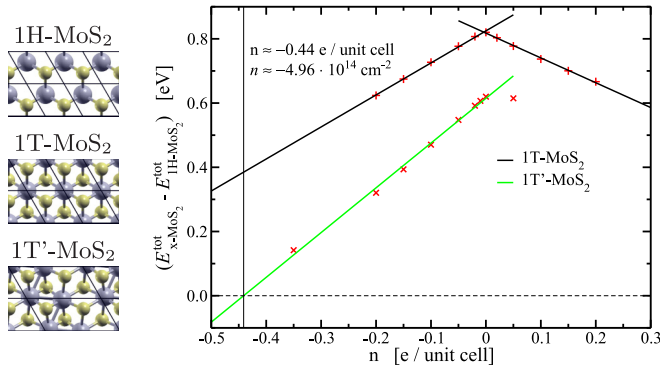
FIG. 4. (Color online) (Left) Structure of three different structural phases of monolayer MoS_2. The H polytype is the one found in the bulk compound where the coordination of the molybdenum (gray) is trigonal prismatic. The T polytype with octahedral coordination can change to the T′ polytype in which the molybdenum atoms form zigzag chains. The sulfur atoms are shown in yellow. (Right) With increasing electron doping the difference between the total energy of 1T/1T′ structure ($E_{\text{x-MoS}_2}^{\text{tot}}$) and the total energy of the 1H polytype ($E_{\text{1H-MoS}_2}^{\text{tot}}$) decreases. For a doping larger than n = −0.44 e/unit cell ($n \approx -4.96 \times 10^{14}$ cm^{-2}) 1T′-MoS_2 is the lowest-energy structure.

D. Band structure in FET setup

In the following section, we want to investigate the influence of field-effect doping on the electronic properties of the TMDs. The doping via FET setup changes the band structure considerably as exemplified in Figs. 5 and 6, which show the band structures for different electron and hole doping levels for monolayer and trilayer MoS_2, respectively. In the Supplemental Material [25] we also demonstrate that it is important to correctly model the FET setup by comparing the band structures of monolayer and trilayer $MoSe_2$ calculated with a compensating jellium background to those calculated with our method (Figs. S7, S8). Furthermore, we also provide the band structures for more doping levels and all the other TMDs in the Supplemental Material [25] (in total more than 250 calculations, Figs. S10–S45). We summarized the evolution of the band structure with increasing doping in the left panel of Figs. 7–11, which show the position of the different band extrema with respect to the Fermi energy. Additionally, the right panel in those figures shows the relative amount of doping charge per valley given by

$$n_\alpha = \frac{e}{N_\alpha} \sum_{\mathbf{k} \in \Omega_\alpha} \sum_{i}^{\varepsilon_1 \leqslant \varepsilon_{i,\mathbf{k}} \leqslant \varepsilon_2} |\psi_{i,\mathbf{k}}|^2. \qquad (6)$$

Here $\alpha = \{\Gamma, K, Q\}$, Ω_α defines the subset of **k** points, which are closer to, e.g., $\alpha = \Gamma$ than to any $\alpha \neq \Gamma$, N_α is the total number of those **k** points, and $\varepsilon_{i,\mathbf{k}}$ is the eigenenergy for band i at **k**. The interval $[\varepsilon_1, \varepsilon_2]$ is always chosen such that the probability density is integrated between an energy within the former band gap E_m and the Fermi energy E_F of the doped system, i.e., $[E_F, E_m]$ and $[E_m, E_F]$ for hole and electron doping, respectively.

1. Electron doping

For n-type doping of monolayer MoS_2 (as for all monolayer TMDs) the doping charge first occupies the extrema at K. For small doping (as long as only one valley is doped) the bands are rigidly shifted. However, as soon as a second valley is close to the Fermi energy, the doping cannot be described by a rigid shift of the bands anymore. For electron doping, the down shift of the bands at K slows down and, as the valley at Q starts to get occupied, is eventually reversed into an up shift. Finally, for high electron doping, the K valley is unoccupied again and the doping charge is solely localized around Q. Comparing our results of the changes in the conduction band for electron doping of monolayer MoS_2 (Figs. 5 and 7) with literature shows that it is important to correctly model the system—while the authors of Ref. [89] find an up shift of the Q valley with increasing electron doping, we see a down shift. The opposite shift in Ref. [89] might be due to the free-electron states at Γ (i.e., the states in the vacuum between the repeated images, cf. also Ref. [90]), which approach the Fermi energy with increasing doping. Also the authors of Refs. [20,23,90] find a down shift of the Q valley further supporting our results even if in those works the asymmetric electric field in an FET has not been taken into account. The amount of doped electrons needed to have the charge completely localized at Q depends on the TMD (i.e., the initial energy difference between the minimum at K and Q) and is larger than $n = -2.2 \times 10^{14}$ cm^{-2} (n ≈ −0.2 e/unit cell): the transition occurs for MoS_2 at $n \approx -3.83 \times 10^{14}$ cm^{-2}, for $MoSe_2$ at $n \approx -2.5 \times 10^{14}$ cm^{-2}, for $MoTe_2$ at $n \approx -2.22 \times 10^{14}$ cm^{-2}, for WS_2 at $n \approx -3.41 \times 10^{14}$ cm^{-2}, and for WSe_2 at $n \approx -3.31 \times 10^{14}$ cm^{-2}. Please note, that using LDA could slightly change these results as it leads to a smaller unit cell. The compressive in-plain strain would then reduce the difference between the conduction-band minima at K and Q [46,47,49] and thus decrease the doping-charge concentration needed to solely dope the valley at Q (cf. Fig. S9).

In multilayer MoS_2, WS_2, and WSe_2 first the valley at K is doped and both valleys at K and Q are occupied until $n \approx -3.3 \times 10^{14}$ cm^{-2} while in bilayer and trilayer $MoSe_2$ and $MoTe_2$ the order is reversed: electrons first occupy the valley at Q and the doping at K is always smaller. This is due to the minimum at Q being lower in energy than the one at K in the undoped system (see Figs. 8 and 9). For a doping of $n \lesssim -2.1 \times 10^{14}$ cm^{-2} for $MoSe_2$ the K valley is even unoccupied. Yet, one can expect that for small electron doping ($|n| < 10^{13}$ cm^{-2}) of thick samples (more than three layers) of MoS_2, WS_2, and WSe_2 the electrons will also first occupy the Q valley as this valley is lowered in energy with increasing number of layers.

2. Hole doping

For p-type doping of the monolayer TMDs, the doping charge first occupies the extrema at K. However, in contrast to the electron-doping case, in the high-hole-doping limit (n > +0.2 e/unit cell, $n \gtrsim +2.1 \times 10^{14}$ cm^{-2}) of the monolayer TMDs both valleys at Γ and K are occupied—the relative amount of doping charge in the Γ valley is even higher than that in K. The transition when the Γ valley is more occupied
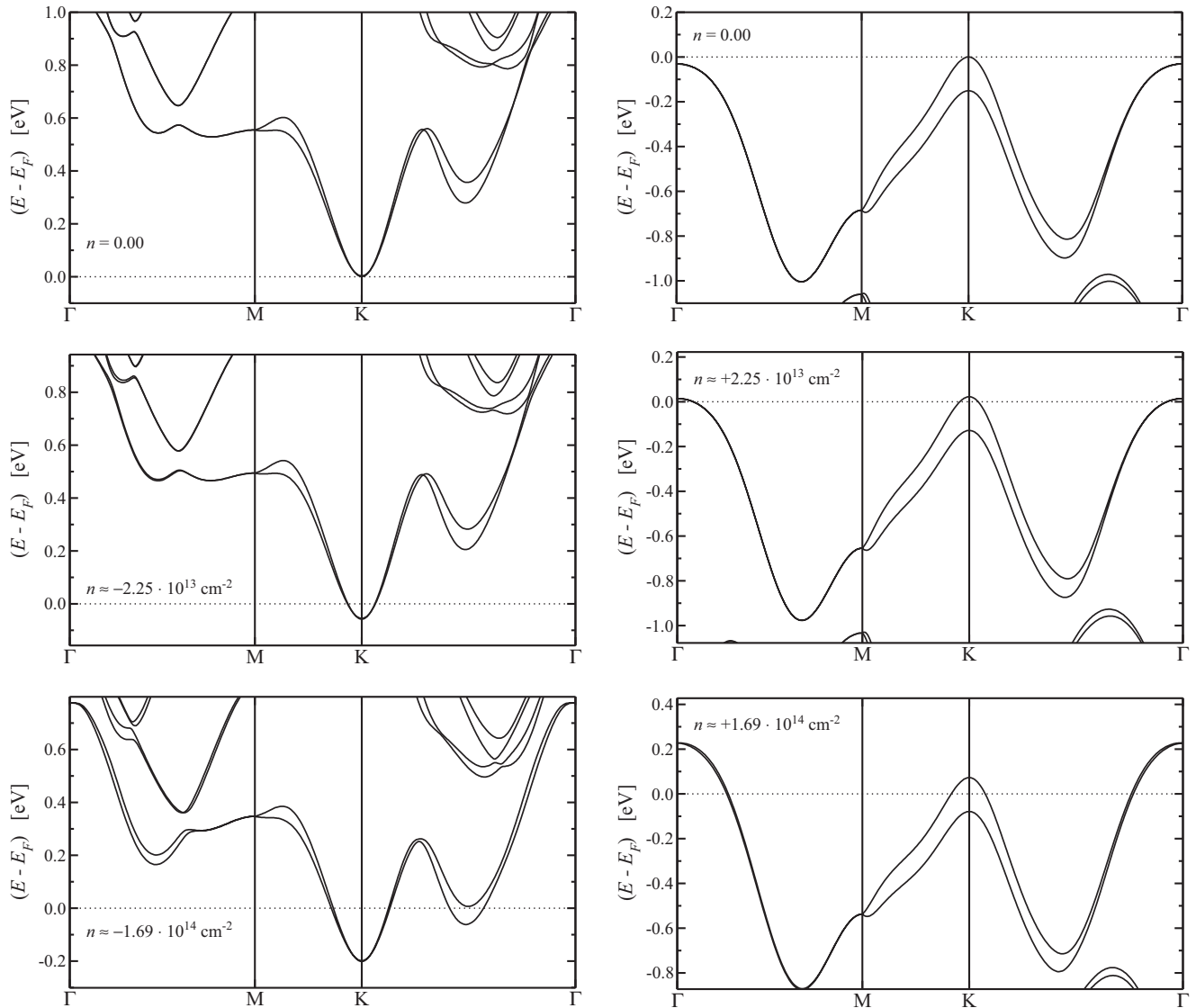
FIG. 5. Band structure for different FET-induced doping of monolayer MoS_2. The figures in the left column are for electron doping while the right column shows the hole-doping case. For monolayer MoS_2 mainly the valleys at K are filled and only for a high doping of $n \approx \pm 1.69 \times 10^{14}$ cm^{-2} ($n = \pm 0.15$ e/unit cell) a small amount of charge is in the maximum at Γ (hole doping) or in the minimum at Q (electron doping). The band structures for more doping levels and all the other TMDs can be found in the Supplemental Material [25] (Figs. S10–S45).

than the K valley again depends on the TMD, i.e., on the initial energy difference between the valence-band maxima. In the case of MoS_2, for example, even a small doping is enough to dope more the Γ valley. The only exception from this picture is $MoTe_2$ for which K is always more occupied even for n = +0.35 e/unit cell ($n \approx +3.23 \times 10^{14}$ cm^{-2}, cf. Fig. 9).

Hole doping of the bilayer and trilayer TMDs is again very similar: in all investigated compounds (except $MoTe_2$) first the conduction-band maximum at Γ is occupied, while for higher doping also K starts to get filled. Most interestingly, in some cases the second band at K is never occupied. For trilayer WS_2 and WSe_2 it is even pushed down in energy, effectively increasing the splitting of the spin-orbit-split bands. For WSe_2 it is possible to achieve even higher hole-doping concentrations than shown in Fig. 11 by using an IL-FET [16].

We thus calculated for trilayer WSe_2 also some higher doping cases (up to n = +1 e/unit cell, or $n \approx +1 \times 10^{15}$ cm^{-2}) in order to understand what might happen for such a high doping. Our calculated band structure is very different from the one in Ref. [16], which was calculated without proper treatment of the FET setup. For a doping of one hole per unit cell the second band at K is pushed down below the Fermi energy and also the first band at K is lowered. The band structure in Fig. 12 shows that the former band gap is closed and the first two bands are nearly unoccupied. However, since these are bands localized on the first layer close to the gate, we believe that for such a high doping the ions of the ionic liquid might start to interact with WSe_2. In our simplified model without inclusion of the full dielectric it is difficult to prove this statement and we will thus leave this interesting problem for future investigations and will concentrate here on lower doping values.
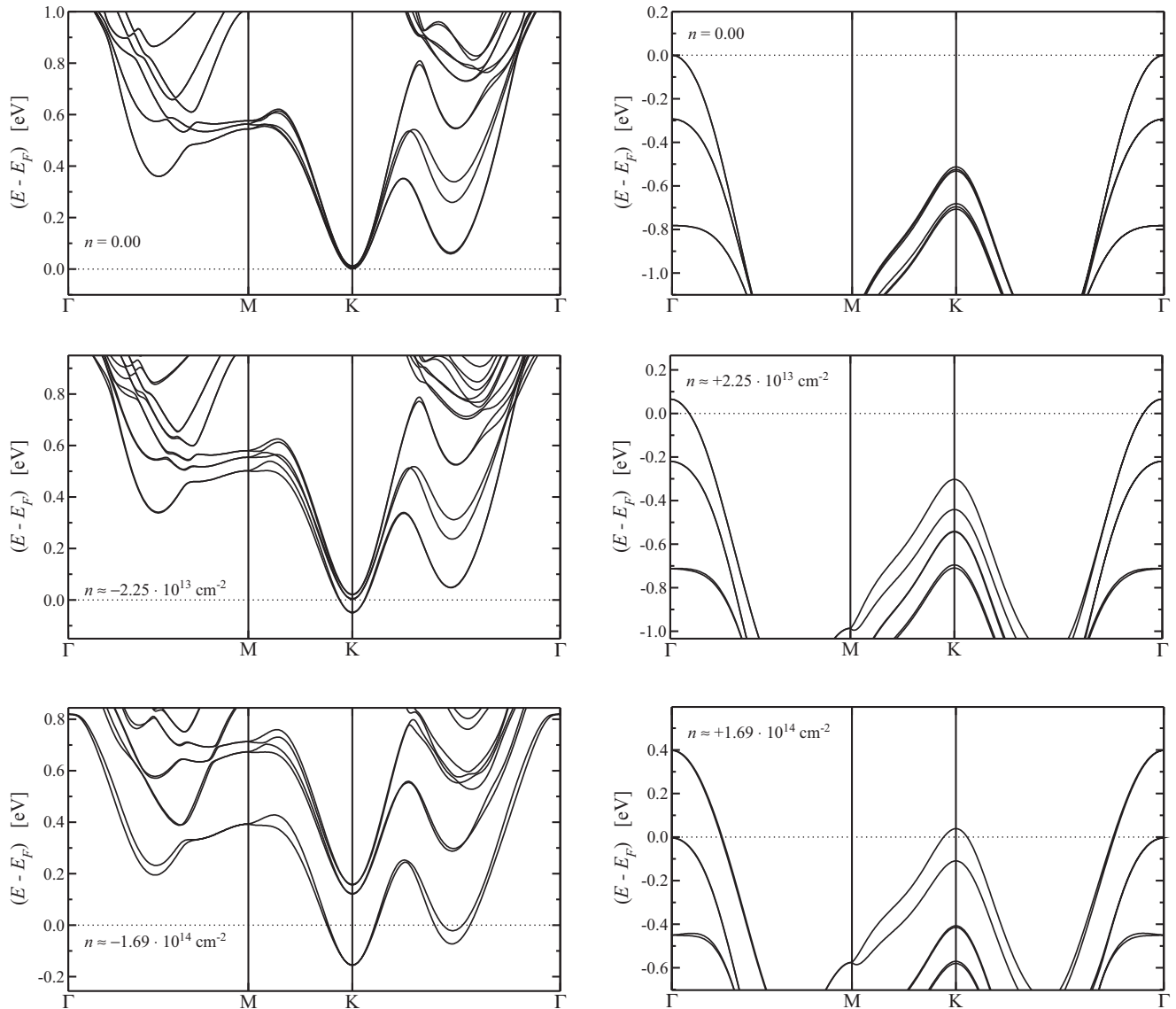
FIG. 6. Band structure for different FET-induced doping of trilayer MoS$_2$. The figures in the left column are for electron doping while the right column shows the hole-doping case. In contrast to the monolayer case, the doping at Γ/Q (hole/electron doping) is more important in trilayer MoS$_2$. The band structures for more doping levels and all the other TMDs can be found in the Supplemental Material [25] (Figs. S10–S45).

3. Conductive channel

Another important property in order to understand different experiments on FET doping on TMDs is the doping-charge layer thickness, i.e., the size and shape of the conductive channel created and influenced by the gate voltage. To visualize the conductive channel we calculated the planar-averaged doping-charge distribution along z,

$$\rho_{||}^{\mathrm{dop}}(z) = \frac{e}{\Omega_{2D} \, N_k} \int dA \sum_{i,\mathbf{k}}^{\varepsilon_1 \leqslant \varepsilon_{i,\mathbf{k}} \leqslant \varepsilon_2} |\psi_{i,\mathbf{k}}(\mathbf{r})|^2. \qquad (7)$$

Here Ω_{2D} is the unit cell area and N_k is the total number of $\mathbf{k}$ points. The interval $[\varepsilon_1, \varepsilon_2]$ is defined as above, i.e., $[E_F, E_m]$ and $[E_m, E_F]$ for hole and electron doping, respectively. This property not only reveals the thickness of the conductive

channel but also the relative distribution among the different layers.

In our calculations for low hole doping the charge is nearly evenly distributed between the first two layers with only small contributions at the third layer as can be seen in the top panel of Fig. 13. Increasing the doping (i.e., increasing the gate voltage, bottom panel of Fig. 13) the charge is more and more localized on the layer closest to the gate with a negligible amount of holes on the third layer. In the case of electron doping of multilayer MoS$_2$, the charge is localized on the first layer as only the K valley is doped (small contribution of the out-of-plane states of sulfur). Only for higher doping when the minimum at Q is occupied, a small amount of charge can be found on the second layer (cf. bottom panel of Fig. 13 and right panel of Fig. 7). One can also see that the asymmetry in the doping-charge distribution is more pronounced for hole doping and that the
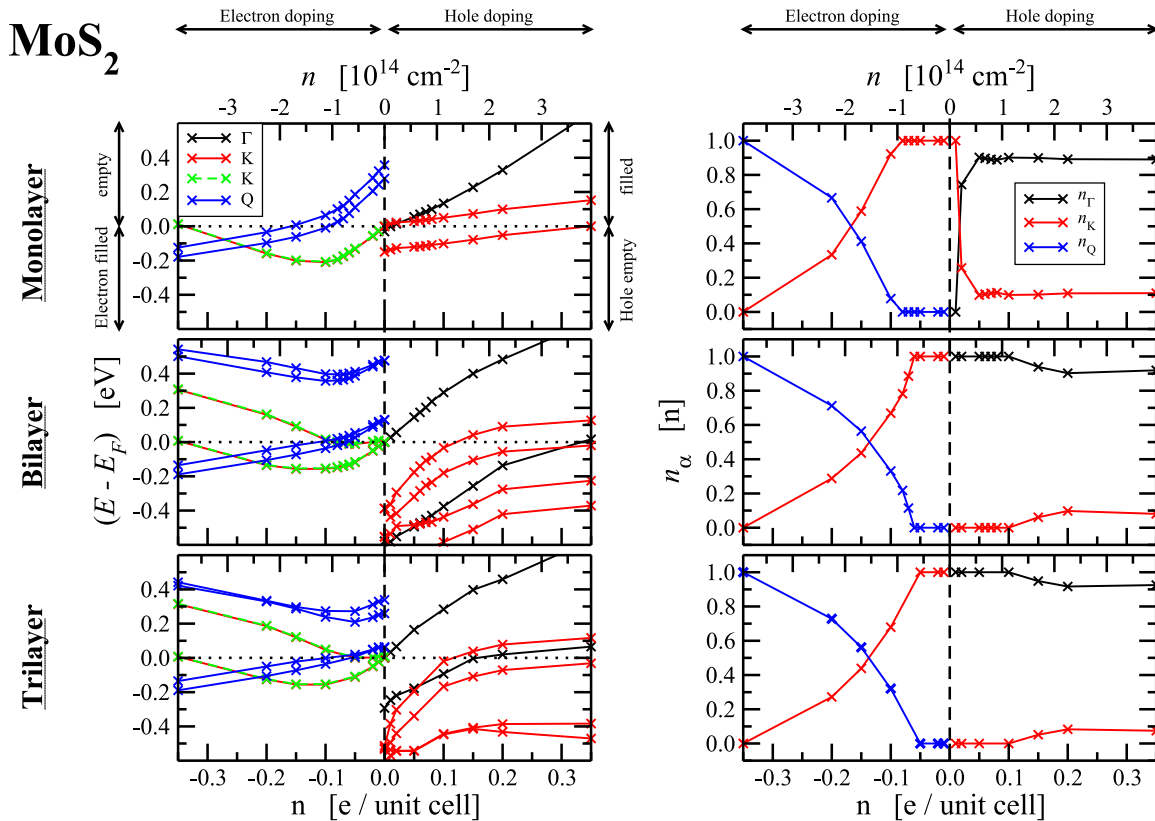
FIG. 7. (Color online) Position of the different band minima/maxima E_i (left) with respect to the Fermi level and relative amount of doping charge per valley n_α (right) as a function of doping for monolayer, bilayer, and trilayer MoS_2. "Q" labels the conduction-band minimum halfway between K and Γ. In each graph, the scale and the units for the lower x axis are given in the lowest graph, while those of the upper x axis are given in the uppermost graph. Two different line styles for the two spin-orbit-split conduction-band minima at K were used in order to enhance the readability. Lines are guides for the eye.

system in this case moves closer to the dielectric. Furthermore, for low hole doping the doping charge on the second layer is even slightly larger than the one on the first.

Figure 14 summarizes the doping-charge distribution for all bilayer and trilayer TMDs. In the hole-doping case all TMDs behave similarly except $MoTe_2$: for low doping the holes are delocalized over the first two layers with only small contributions in the third layer and, thus, the bilayer and trilayer systems are nearly the same. Increasing the doping leads to stronger localization of the charge within the first layer and an effective narrowing of the conductive channel. One can also easily understand why $MoTe_2$ behaves differently: in all multilayer TMDs first the valley at Γ is doped, since it is the valence-band maximum, while in $MoTe_2$ the K valley is the maximum. As we have seen in Sec. III A the states close to Γ have large out-of-plane contributions of both the transition-metal and the chalcogen atom, while the valley at K is composed only of in-plane states. Increasing the hole doping however also leads for $MoTe_2$ to a small doping of the Γ valley. Thus, the amount of charge within the second layer increases slightly in the beginning. The small kink for trilayer $MoTe_2$ close to $n = +0.46 \times 10^{14}$ cm^{-2} is due to both bands at Γ and K being close to the Fermi energy. In this low-doping limit (per valley) the calculation would require an infinite number of **k** points to fully converge the results. Further increase of the doping leads, as for all TMDs, to a larger screening of the

electric field and therefore to the stronger localization within the first layer as can also be seen in the bottom panel Fig. 13.

For electron doping we can divide the different TMDs into two different classes: (i) those in which the conductive channel for low doping ($n \approx -10^{13}$ cm^{-2}) has a thickness of just one layer (MoS_2, WS_2, WSe_2) and (ii) those with a three-layer-thick channel ($MoSe_2$, $MoTe_2$). Using the results of Figs. 7–11 one can see that in the TMDs of class (i) initially the K valley is doped while in (ii) the Q valley is occupied. Since the chalcogen states close to the conduction-band minimum at K have mainly in-plane character (in contrast to the transition-metal states, which have d_{z^2} character), the hybridization between the layers is small and the electrons are more localized within the first layer. The chalcogen states close to Q on the other hand have a large out-of-plane contribution, which leads to a stronger hybridization between the layers. With increasing doping the electric field of the gate is more and more screened and the size of the conductive channel reduces to one layer. Furthermore, one can also understand why the tungsten dichalcogenides have a steep increase of the channel thickness in the beginning while this is not the case for MoS_2: first, the difference between the conduction-band minimum at K and Q is much smaller in multilayer WS_2/WSe_2 than in MoS_2 and second, a small electron doping can also results in an effective separation of the single (doped) layer from the multilayer system. The difference between the conduction-band
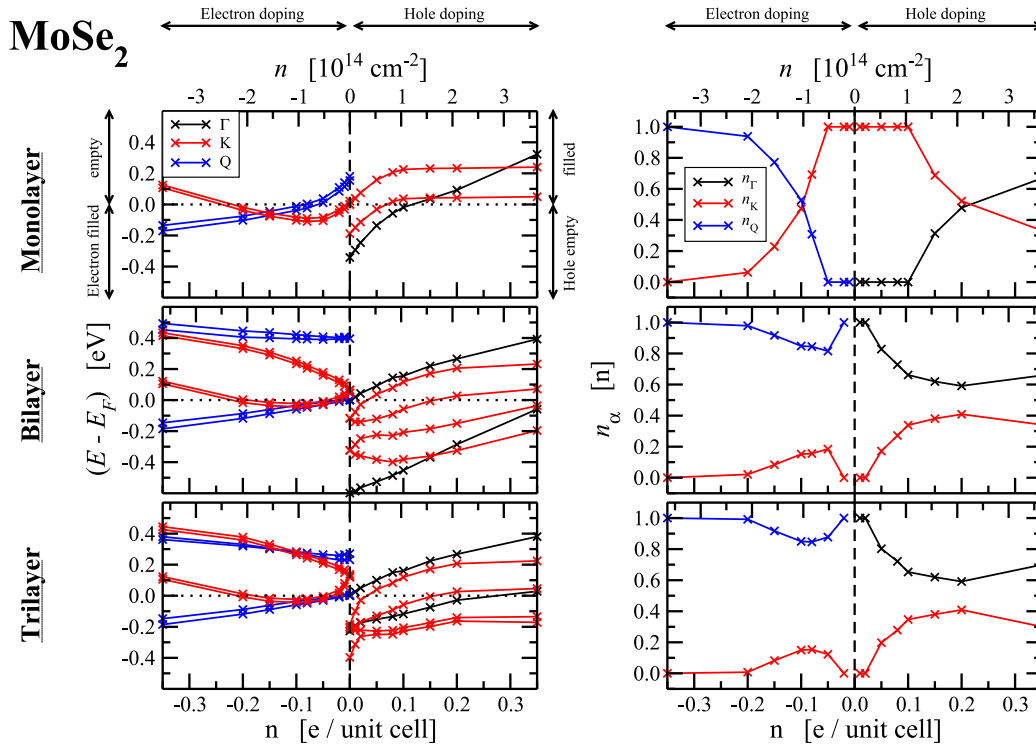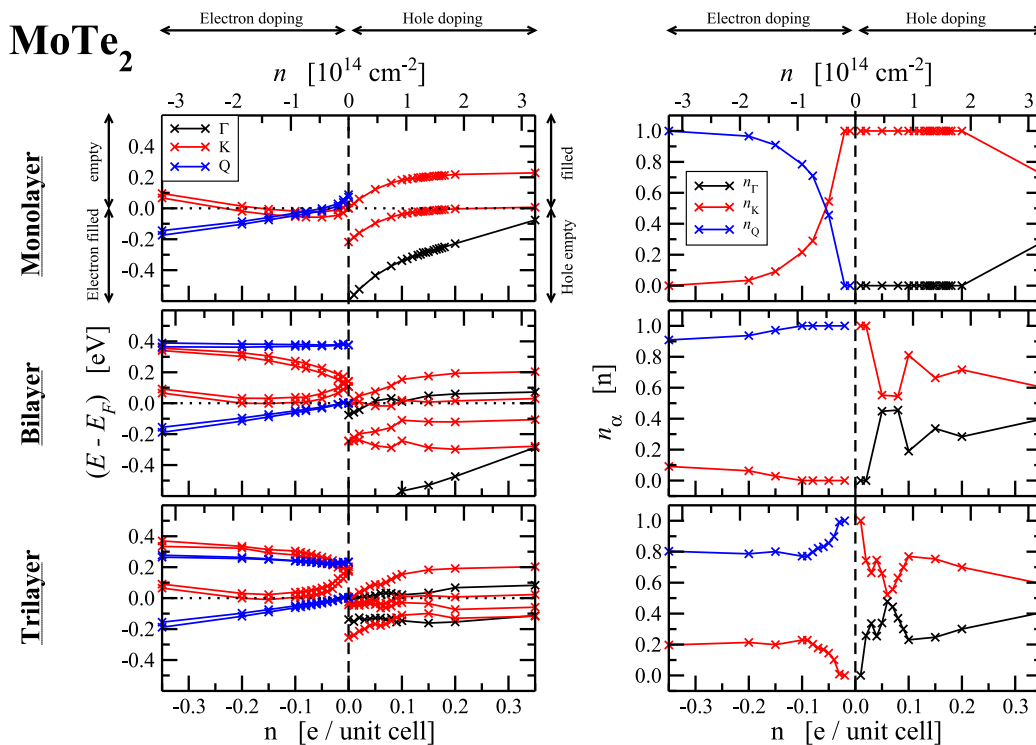
FIG. 8. (Color online) Position of the different band minima/maxima E_i (left) with respect to the Fermi level and relative amount of doping charge per valley n_α (right) as a function of doping for monolayer, bilayer, and trilayer MoSe$_2$. "Q" labels the conduction-band minimum halfway between K and Γ. In each graph, the scale and the units for the lower x axis are given in the lowest graph, while those of the upper x axis are given in the uppermost graph. Lines are guides for the eye.
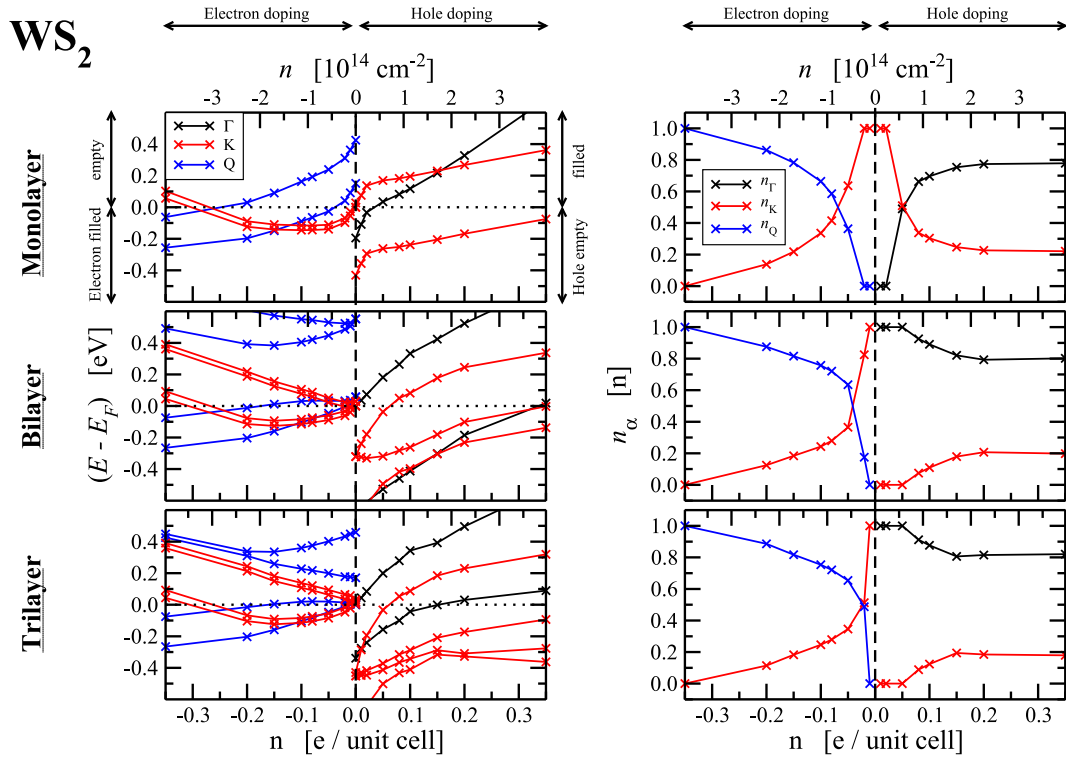

FIG. 9. (Color online) Position of the different band minima/maxima E_i (left) with respect to the Fermi level and relative amount of doping charge per valley n_α (right) as a function of doping for monolayer, bilayer, and trilayer MoTe$_2$. "Q" labels the conduction-band minimum halfway between K and Γ. In each graph, the scale and the units for the lower x axis are given in the lowest graph, while those of the upper x axis are given in the uppermost graph. Lines are guides for the eye.
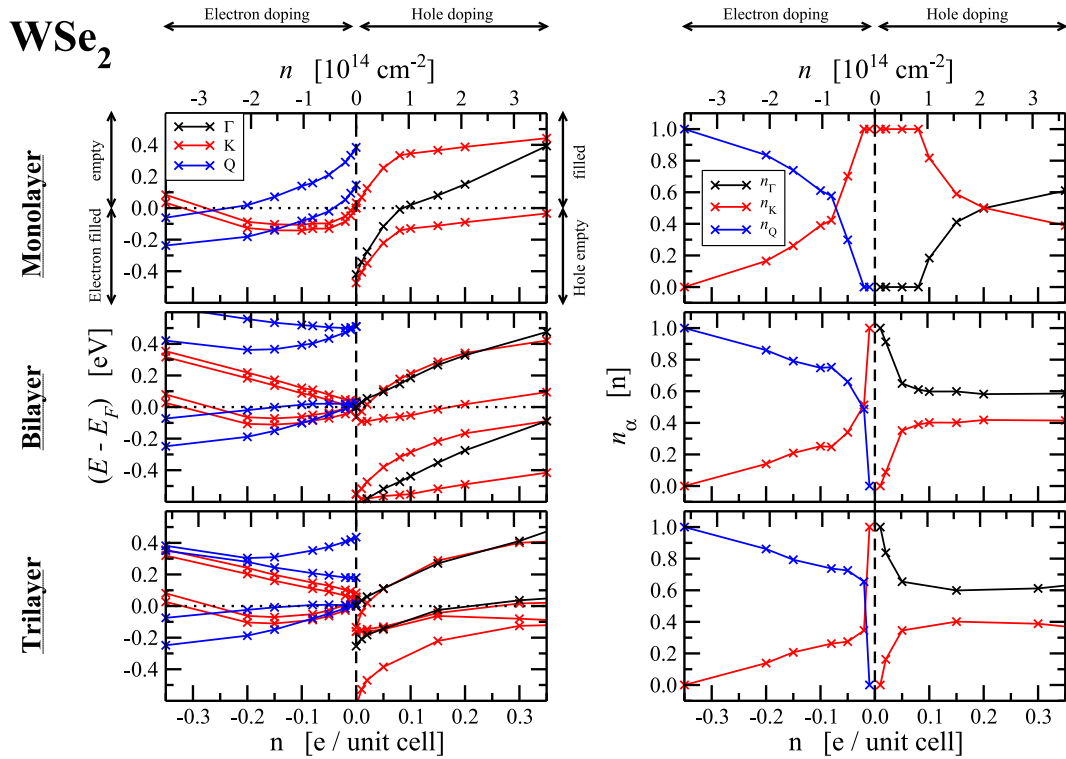
FIG. 10. (Color online) Position of the different band minima/maxima E_i (left) with respect to the Fermi level and relative amount of doping charge per valley n_α (right) as a function of doping for monolayer, bilayer, and trilayer WS_2. "Q" labels the conduction-band minimum halfway between K and Γ. In each graph, the scale and the units for the lower x axis are given in the lowest graph, while those of the upper x axis are given in the uppermost graph. Lines are guides for the eye.

FIG. 11. (Color online) Position of the different band minima/maxima E_i (left) with respect to the Fermi level and relative amount of doping charge per valley n_α (right) as a function of doping for monolayer, bilayer, and trilayer WSe_2. "Q" labels the conduction-band minimum halfway between K and Γ. In each graph, the scale and the units for the lower x axis are given in the lowest graph, while those of the upper x axis are given in the uppermost graph. Lines are guides for the eye.
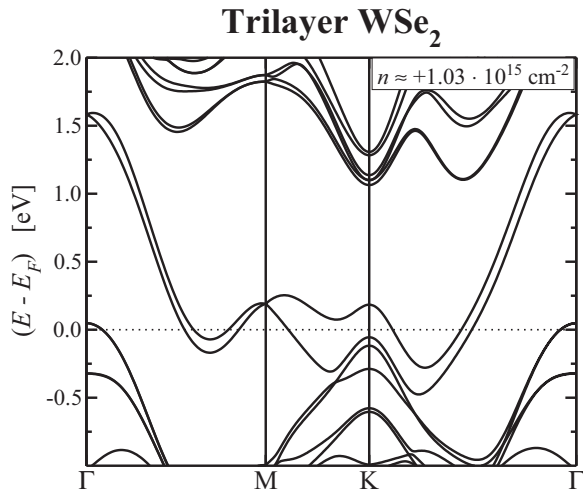
FIG. 12. Band structure of trilayer WSe_2 for a high hole doping of $n \approx +1.03 \times 10^{15}$ cm^{-2} (n = +1 e/unit cell).

minimum at K and Q for monolayer MoS_2 is, however, twice as large as in the tungsten systems (≈ 300 meV for MoS_2 and ≈ 150 meV for WS_2/WSe_2). Thus, the valley at the Q point is doped much earlier in WS_2/WSe_2 than in MoS_2.

4. Number of occupied bands

It is important to note that the thickness of the doping-charge distribution, the number of occupied bands at a given **k** point, and the number of TMD layers (i.e., the system size) are uncorrelated. Indeed, as can be seen in Fig. 15, the total spin-valley degeneracy ν can be quite similar for different number of layers, whereas the doping charge is localized on one or two layers as seen in the previous section. Here the
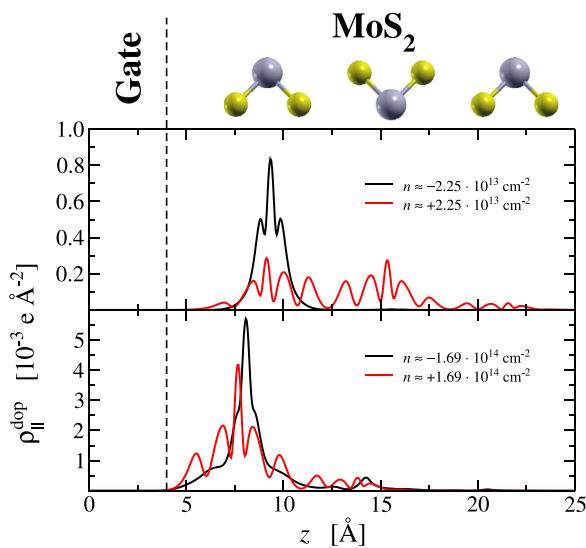

FIG. 13. (Color online) Planar-averaged doping-charge distribution along z for trilayer MoS_2 for a doping of $n \approx \pm 2.25 \times 10^{13}$ cm^{-2} (n = ± 0.02 e/unit cell, upper panel) and $n \approx \pm 1.69 \times 10^{14}$ cm^{-2} (n = ± 0.15 e/unit cell, lower panel). The dashed line within the graph indicates the end of the barrier potential, while the sketch above shows the position of the atoms (gray: Mo, yellow: S).
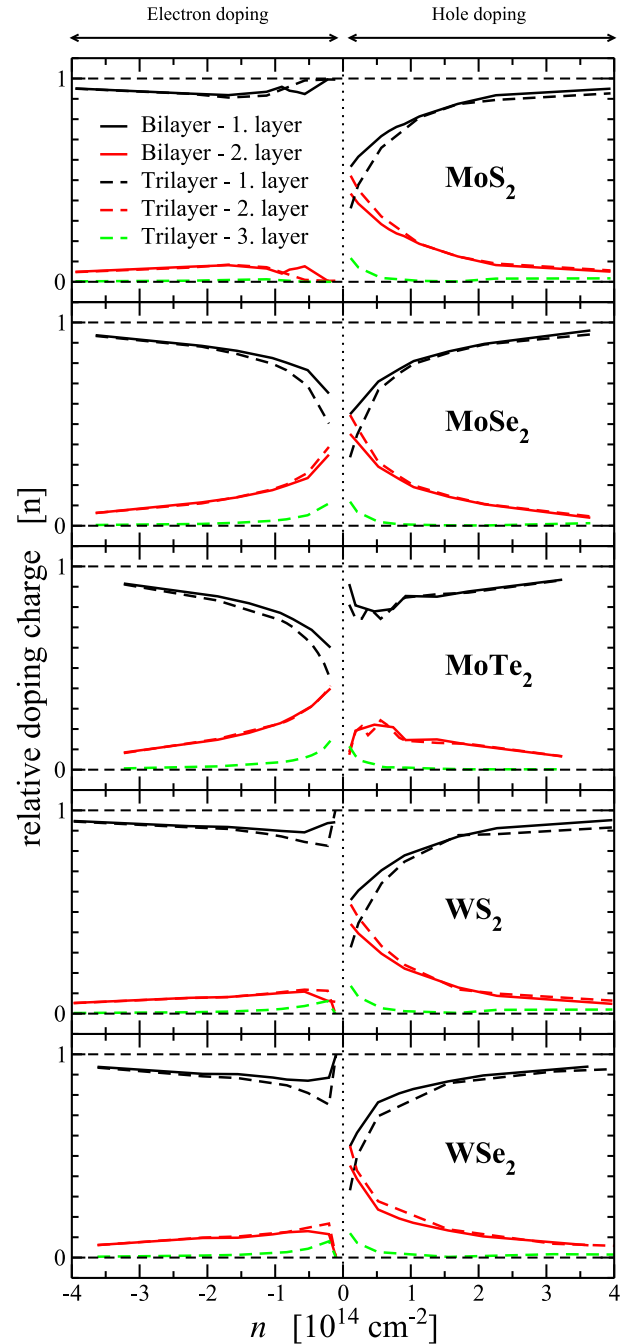

FIG. 14. (Color online) Relative doping charge per layer for bilayer and trilayer of the different dichalcogenides with increasing FET doping.

total spin-valley degeneracy has been calculated by counting the number of valleys within the interval $[\varepsilon_1, \varepsilon_2]$ as defined above:

$$\nu = \sum_\alpha \nu^\alpha = \sum g_s^\alpha g_v^\alpha. \tag{8}$$

Here g_s^α and g_v^α are the spin and valley degeneracies of the valley at **k** point $\alpha = \{\Gamma, K, Q\}$. For electron doping ν is much higher than in the hole-doping case as the valley degeneracy for the conduction-band minimum close to Q is $g_v = 6$ (spin degeneracy $g_s = 1$). Thus, as soon as the valley at Q is doped,
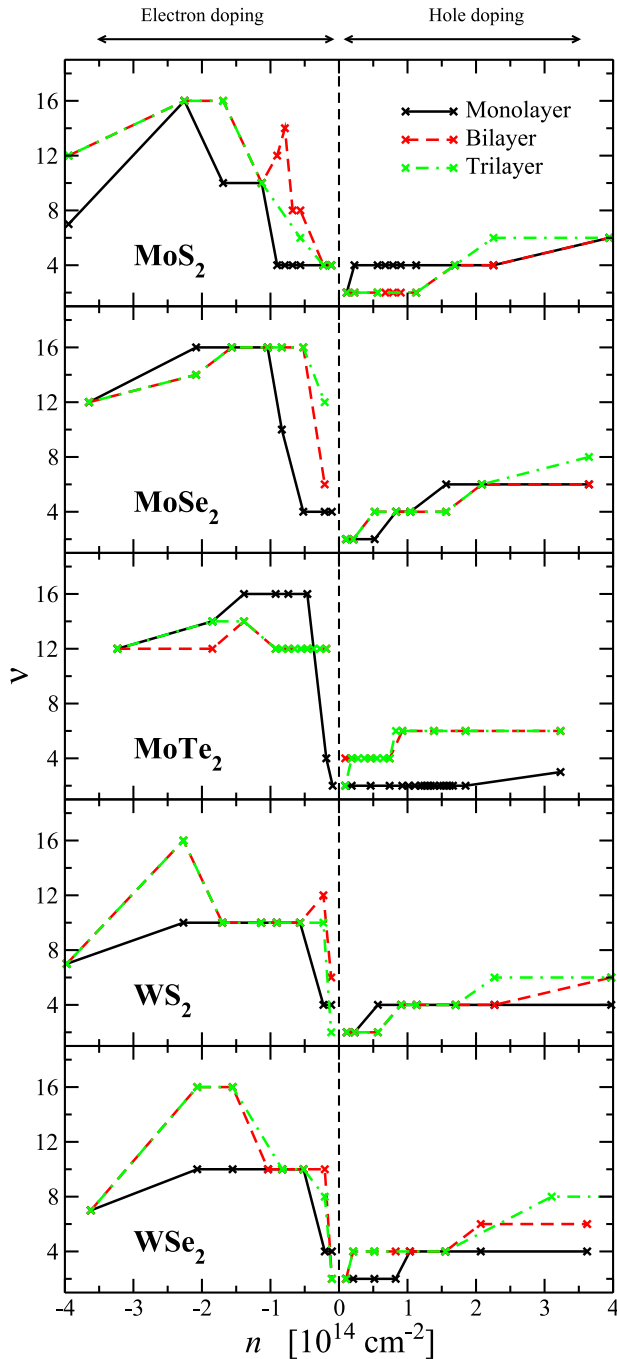
FIG. 15. (Color online) Total spin-valley degeneracy ν as a function of doping for the monolayer, bilayer, and trilayer system of all investigated TMDs. The total spin-valley degeneracy has been calculated by summing the spin and valley degeneracies of all doped valleys. Lines are guides for the eye.

ν increases drastically by 6 or 12 depending on whether only one or both spin-orbit-split bands are filled. For some TMDs a high electron doping of $n < -3.5 \times 10^{14}$ cm^{-2} leads to a large lowering of the minimum at Q—so much that it is actually not a valley anymore but a ring around Γ. This can be seen by the minimum between Γ and M, which appears in the band structure (cf. Figs. 5 and 6 and band structures in the

Supplemental Material [25]). In this case, we do not count it as six independent valleys but as one.

In contrast, for high hole doping ($n \gtrsim +2 \times 10^{14}$ cm^{-2}) of multilayer TMDs the number of occupied valleys is either $\nu = 6$ or $\nu = 8$ as only bands at K ($g_v = 2$, $g_s = 1$) and Γ ($g_v = 1$, $g_s = 2$) are doped. In the monolayer systems often two valleys are doped—the valence-band maximum at K and either the second spin-orbit-split band at K or the valence-band maximum at Γ. Accordingly, the difference between the valence-band maximum at K and at Γ determines the doping-charge concentration needed in order to dope two valleys at different points in the BZ. The spin-degenerate maximum at Γ is occupied for monolayer MoS$_2$, MoSe$_2$, WS$_2$, and WSe$_2$ for hole doping larger than $+1 \times 10^{13}$ cm^{-2}, $+5 \times 10^{13}$ cm^{-2}, $+2 \times 10^{13}$ cm^{-2}, and $+8 \times 10^{13}$ cm^{-2}, respectively. Again monolayer MoTe$_2$ is exceptional due to the large difference of ≈ 600 meV between the maximum at K and Γ. Just for a very high hole doping of $n \approx +3.23 \times 10^{14}$ cm^{-2} (n = $+0.35$ e/unit cell) the second band at K is occupied and a ring around and close to Γ appears (which is again counted as 1).

Up to now we have focused on the changes in the electronic structure of the different TMDs with increasing doping and we saw that for, e.g., high electron doping the charge is mainly localized around the Q point. We now want to investigate how the amount of doping charge and thus the number of occupied bands and the thickness of the conductive channel is determined experimentally.

E. Hall-effect measurements

In order to determine the doping charge in a sample, one commonly performs a Hall experiment as the inverse Hall coefficient is directly proportional to the charge-carrier density n in the case of parabolic, isotropic bands. This, however, is already a crude approximation, which, as we will see below, can lead to large differences between the charge-carrier density thus calculated and the real density within the sample.

We closely follow the work of Madsen and Singh [45] and sketch the calculation of the Hall coefficient (or more specifically, the Hall tensor R_{ijk}) within Boltzmann transport theory. In the presence of an electric field **E** and a magnetic field **B**, the electric current **j** can be written as

$$j_\alpha = \sigma_{\alpha\beta} E_\beta + \sigma_{\alpha\beta\gamma} E_\beta B_\gamma + \cdots, \tag{9}$$

with the conductivity tensors $\sigma_{\alpha\beta}$ and $\sigma_{\alpha\beta\gamma}$, and the indices denoting the spatial dimensions. Here and henceforth, we will always adopt Einstein's sum convention, according to which whenever an index occurs twice in a single-term expression, the summation is carried out over all possible values of this index. The Hall tensor is defined as

$$R_{ijk}(T; E_F) = \frac{\mathbf{E}_j^{\text{ind}}}{\mathbf{j}_i^{\text{appl}} \mathbf{B}_k^{\text{appl}}} = (\sigma^{-1})_{\alpha j}\, \sigma_{\alpha\beta k}\, (\sigma^{-1})_{i\beta}, \tag{10}$$

where $\mathbf{E}_j^{\text{ind}}$ is the electric field along direction j, which is induced by the applied magnetic field $\mathbf{B}_k^{\text{appl}}$ and current $\mathbf{j}_i^{\text{appl}}$ along direction k and i, respectively.

Within the relaxation-time approximation the conductivity tensors $\sigma_{\alpha\beta}$ and $\sigma_{\alpha\beta\gamma}$ for temperature T and chemical potential

E_F are given in the 2D case by [45]

$$\sigma_{\alpha\beta}(T; E_F) = \frac{q^2}{(2\pi)^2} \int \tau_{i,\mathbf{k}} \, v_\alpha^{i,\mathbf{k}} \, v_\beta^{i,\mathbf{k}} \left[-\frac{\partial f_{E_F}(T; \varepsilon_{i,\mathbf{k}})}{\partial \varepsilon} \right] d^2\mathbf{k},$$
(11)

$$\sigma_{\alpha\beta\gamma}(T; E_F) = \frac{q^3}{(2\pi)^2} \int \tau_{i,\mathbf{k}}^2 \, \epsilon_{\gamma u v} \, v_\alpha^{i,\mathbf{k}} \, v_\nu^{i,\mathbf{k}} \left(M_{\beta u}^{i,\mathbf{k}} \right)^{-1}$$
$$\times \left[-\frac{\partial f_{E_F}(T; \varepsilon_{i,\mathbf{k}})}{\partial \varepsilon} \right] d^2\mathbf{k}.$$
(12)

Here, $q = \pm e$ is the charge of the charge carriers in band $\varepsilon_{i,\mathbf{k}}$ with momentum $\mathbf{k}$, $f_{E_F}(T; \varepsilon)$ is the Fermi function $f_{E_F}(T; \varepsilon) = (\exp[(\varepsilon - E_F)/(k_B T)] + 1)^{-1}$, and $\epsilon_{\gamma u v}$ is the Levi-Civita symbol. The relaxation time $\tau_{i,\mathbf{k}}$ in principle is dependent on both the band index i and the $\mathbf{k}$-vector direction. Furthermore, $v_\alpha^{i,\mathbf{k}}$ is the group velocity

$$v_\alpha^{i,\mathbf{k}} = \frac{1}{\hbar} \frac{\partial \varepsilon_{i,\mathbf{k}}}{\partial k_\alpha}$$
(13)

and $(M_{\beta u}^{i,\mathbf{k}})^{-1}$ the inverse mass tensor

$$\left(M_{\beta u}^{i,\mathbf{k}} \right)^{-1} = \frac{1}{\hbar^2} \frac{\partial^2 \varepsilon_{i,\mathbf{k}}}{\partial k_\beta \partial k_u}.$$
(14)

To show that the inverse Hall coefficient R_{xyz} is proportional to n, we start by assuming bands with quadratic dispersion. The dispersion relation for a quadratic, isotropic band in two dimensions is given by

$$\varepsilon_{i,k} = \frac{\hbar^2 k^2}{2 m_i},$$
(15)

with $k^2 = k_x^2 + k_y^2$. The group velocity is then $v_\alpha^{i,k_\alpha} = \hbar k_\alpha / m_i$ while the mass tensor in Eq. (14) is for each band a diagonal matrix with m_i^{-1} on the diagonal. In the zero-temperature limit and assuming an i- and $\mathbf{k}$-independent relaxation time $\tau_{i,\mathbf{k}} = \tau(E_F)$ the conductivity distributions in Eqs. (11) and (12) are given by

$$\sigma_{\alpha\alpha}(0; E_F) = \sum_i \frac{q^2 \tau}{m_i} n_i,$$
(16)

$$\sigma_{\alpha\beta\gamma}(0; E_F) = -\sum_i \frac{q^3 \tau^2}{m_i^2} \epsilon_{\alpha\beta\gamma} n_i,$$
(17)

where n_i is the charge-carrier density in band i. Finally, assuming that the magnetic field is applied perpendicular to the 2D system along z, we get for the Hall coefficient

$$R_{xyz}(0; E_F) = \frac{\sum_i m_i^{-2} n_i}{q \left(\sum_i m_i^{-1} n_i \right)^2}.$$
(18)

Thus, only for valley-independent effective mass $m_i = m$ the inverse Hall coefficient is directly proportional to the doping-charge concentration $n = nq$. The results in Eqs. (16), (17), and (18) also hold for a 3D system, however with the important difference that the conductivity in two dimensions is independent of the mass of the charge carriers, since the density n is proportional to m. Furthermore, the Hall coefficient is inversely proportional to the mass m in the 2D case.

In the constant-relaxation-time approximation [$\tau_{i,\mathbf{k}} = \tau(E_F)$] and for hexagonal symmetry (such as in the TMDs), the Hall tensor in Eq. (10) has only two independent coefficients [91] (in-plane and out-of-plane component). However, it is important to remember that this simple equation for the Hall coefficient R_{xyz}, Eq. (18), is only valid as long as there are only bands with isotropic, quadratic dispersion and if $\tau_{i,\mathbf{k}} = \tau(E_F)$. For small doping this might be a good approximation but in the high-doping case this approximation can break down—especially, as soon as a minimum/maximum with nonquadratic dispersion starts to get filled.

Figure 16 shows the ratio of the inverse Hall coefficient $R_{xyz}^{-1}(T; E_F)$ [calculated with the BOLTZTRAP code [45] using Eqs. (10)–(12) and assuming $\tau_{i,\mathbf{k}} = \tau(E_F)$] to the doping-charge concentration n, as a function of doping for the monolayer, bilayer, and trilayer systems for $T = 300$ K. The comparison between $T = 0$ K and $T = 300$ K, which can be found in the Supplemental Material [25], Figs. S46–S48, shows that the temperature has only a minor influence on the inverse Hall coefficient except for MoTe$_2$ (which we will also discuss separately).

For most of the studied systems, the inverse Hall coefficient $R_{xyz}^{-1}(300$ K$; E_F)$ shows a strong deviation from the doping charge n for large doping—the doping-charge concentration calculated using the inverse Hall coefficient can be 1.5 times larger than the real concentration. In fact, $R_{xyz}^{-1}(300$ K$; E_F) \approx$ n is true only in two cases [cf. Eq. (18)]: either (i) if mainly one valley with parabolic dispersion is doped or (ii) if the doping charge is split between several valleys with quadratic bands, which, however, have similar effective masses.

Case (i) holds only for small hole doping ($n \lesssim +5 \times 10^{13}$ cm^{-2}) of all multilayer TMDs as mainly the Γ valley is doped. The deviation of the inverse Hall coefficient from the doping charge n increases with increasing doping of the valence-band maximum at K. Accordingly, $R_{xyz}^{-1}(300$ K$; E_F) \approx$ n for a larger range of hole doping of multilayer MoS$_2$ than in the other TMDs as the doping at K is negligible. For high hole doping ($n \gtrsim +2 \times 10^{14}$ cm^{-2}) the deviation is due to the nonparabolicity of the bands near K. If, however, the charge is split between Γ and K the difference can be explained by the much larger effective mass of the Γ valley [i.e., in variance with case (ii)]. Assuming $n_\Gamma \approx n_K = n/2$, the ratio of the inverse Hall coefficient to the doping charge [cf. Eq. (18)] simplifies to

$$\frac{R_{xyz}(0; E_F)^{-1}}{n} = \frac{1}{2} + \frac{m_\Gamma m_K}{m_\Gamma^2 + m_K^2},$$
(19)

which is always smaller than 1 for $m_\Gamma \neq m_K$. This also explains why the ratio approaches ≈ 0.7 for small hole doping of monolayer MoS$_2$. At $T = 300$ K the charge n is split between both maxima which have however very different masses [47]—$m_\Gamma = 3.524 \, m_0$ and $m_K = 0.637 \, m_0$.

The agreement between $R_{xyz}^{-1}(300$ K$; E_F)$ and n is much better for electron doping up to $n \approx -2 \times 10^{14}$ cm^{-2} even if both conduction-band minima at K and Q are occupied. This is due to the similar effective masses of those two valleys. As in the hole-doping case the difference between $R_{xyz}^{-1}(300$ K$; E_F)$ and n increases for larger doping ($n \lesssim -2 \times 10^{14}$ cm^{-2}), which is due to the increasing nonparabolicity of the bands.
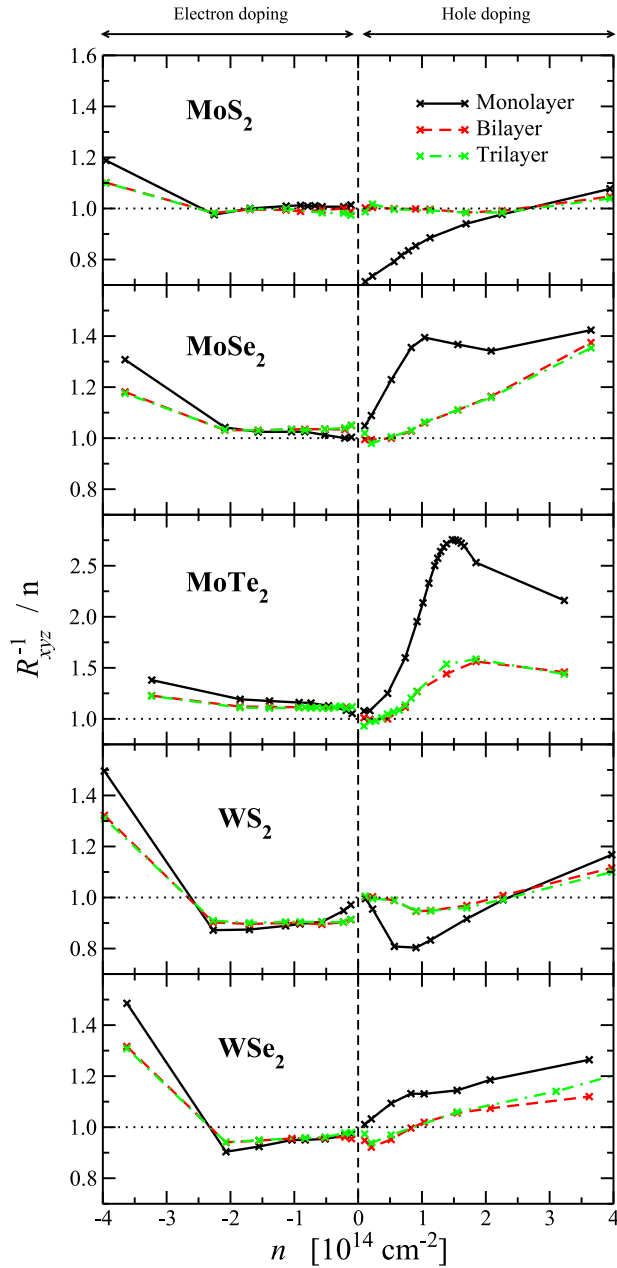
FIG. 16. (Color online) Ratio of the inverse Hall coefficient R_{xyz}^{-1} to the doping charge n as a function of doping for the monolayer (black, solid), bilayer (red, dashed), and trilayer (green, dash-dotted) of all investigated TMDs for a temperature of $T = 300$ K. Note also the different range of the ordinate in the case of MoTe$_2$.

The only case where the model of a 2D electron gas with constant relaxation time gives reasonable results for the doping-charge concentration within a large range of both electron and hole concentrations is multilayer MoS$_2$. Since the agreement between $R_{xyz}^{-1}(T; E_F)$ and n can be much better in other systems as exemplified for CoSb$_3$ in Ref. [45], the deviations shown in Fig. 16 point out problems if the specific band structure is not taken into account. Once again, MoTe$_2$ is particularly interesting because the inverse Hall coefficient $R_{xyz}^{-1}(300 \text{ K}; E_F)$ is nearly three times bigger than n for a hole doping of $n \approx +1.4 \times 10^{14}$ cm^{-2}.
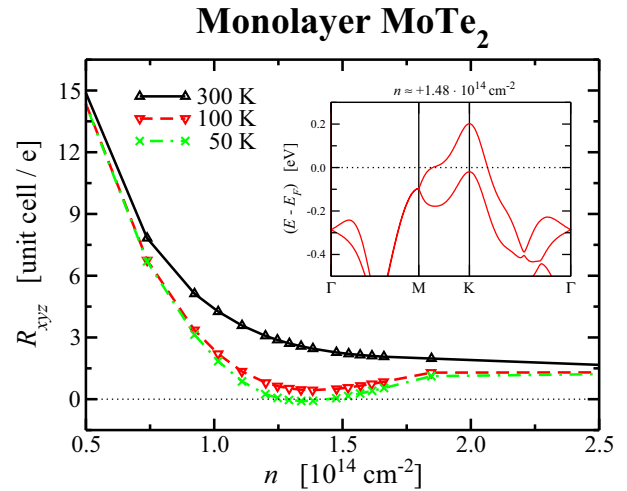

FIG. 17. (Color online) Hall coefficient R_{xyz} as a function of doping for monolayer MoTe$_2$ and temperatures $T = 300$ K, $T = 100$ K, and $T = 50$ K. The inset shows the band structure for a critical doping of $n \approx 1.48 \times 10^{14}$ cm^{-2} (n = +0.16 e/unit cell). The specific band structure of MoTe$_2$ with the nearly linear dispersion along $K \to \Gamma$ and the changing sign of the effective mass when increasing the distance to K leads to the large difference between R_{xyz}^{-1} and n.

In order to understand the origin of this behavior of R_{xyz}^{-1}/n for hole doping of monolayer MoTe$_2$, we plot R_{xyz} as a function of temperature in Fig. 17. As the temperature is reduced, the Hall coefficient $R_{xyz}(T; E_F)$ decreases and for $T \leqslant 50$ K it even changes the sign. The result for $T = 50$ K in Fig. 17 indicates that in the range of $+1.25 \times 10^{14}$ cm$^{-2} \leqslant n \leqslant +1.5 \times 10^{14}$ cm^{-2} the Hall coefficient R_{xyz} changes twice the sign. The band structure for a doping of $n \approx +1.48 \times 10^{14}$ cm^{-2} (inset in Fig. 17) shows that the valence band has at least two inflection points close to the K point, which cross the Fermi energy with increasing doping. Accordingly, the effective mass changes the sign and thus also the conductivity tensor $\sigma_{\alpha\beta\gamma}$ and R_{ijk}. Furthermore, the nearly linear dispersion along $K \to \Gamma$ leads to $m \to 0$ and thus to the large difference between R_{xyz}^{-1} and n. For bilayer and trilayer MoTe$_2$ the deviations are smaller and at higher doping values. This is due to the finite contribution of the doping charge at the Γ point, which leads to a smaller doping around K.

F. Conductivity and DOS at the Fermi energy

In the end, we want to briefly analyze the DOS at the Fermi energy E_F and the in-plane conductivity σ_{xx}/τ in Fig. 18. Both were calculated using the fitted band structure of BOLTZTRAP. The DOS at the Fermi energy E_F in the left-hand panel shows that the doping charge cannot always be described with quadratic, isotropic bands in two dimensions (as also shown above by the behavior of R_{xyz}^{-1}). In this case, DOS(E_F) would be constant and would have steps as soon as another band crosses E_F. In fact, DOS(E_F) has steps and those can be related to crossing bands, but for high doping it can deviate from a simple 2D electron gas.

For hole doping of monolayer MoS$_2$, MoSe$_2$, WS$_2$, and WSe$_2$ the DOS at the Fermi energy is nearly constant as
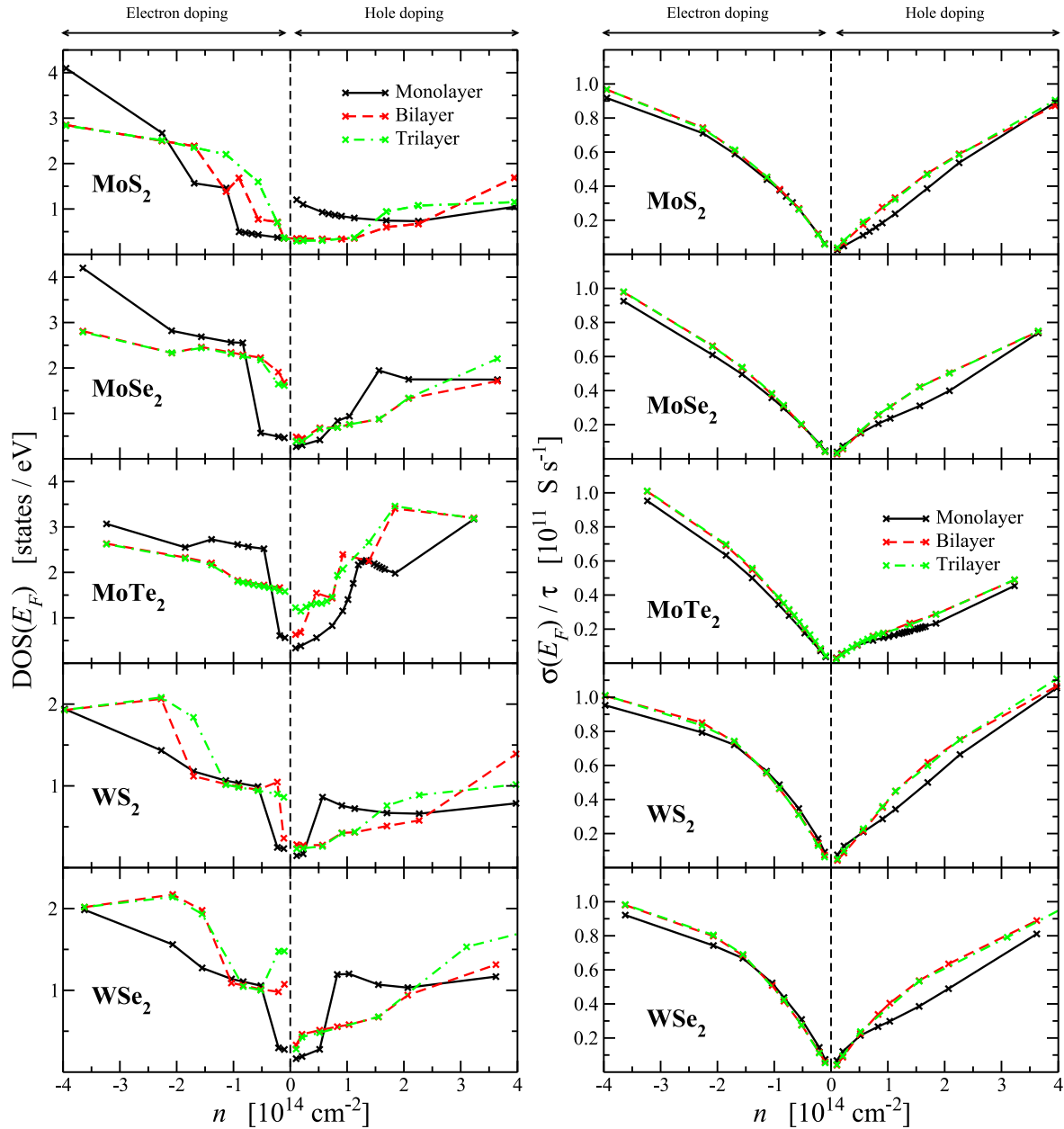
FIG. 18. (Color online) DOS at the Fermi energy E_F (left, $T = 0$ K) and in-plane conductivity σ_{xx}/τ (right, $T = 300$ K) as a function of doping for the monolayer (black, solid), bilayer (red, dashed), and trilayer (green, dash-dotted) of all investigated TMDs. Note also the different range of the ordinate for DOS(E_F) in the case of WS$_2$ and WSe$_2$. Lines are guides for the eye.

soon as the Γ valley is doped, i.e., for doping larger than $n \approx +0.1 \times 10^{14}$ cm^{-2}, $n \approx +1.5 \times 10^{14}$ cm^{-2}, $n \approx +0.5 \times 10^{14}$ cm^{-2}, and $n \approx +0.9 \times 10^{14}$ cm^{-2}, respectively. Also for hole doping smaller than $n \leqslant +1.1 \times 10^{14}$ cm^{-2} of multilayer MoS$_2$ the DOS is constant as only the Γ valley is doped in this regime. The nonconstant behavior for hole doping of the other multilayer systems increases with increasing doping of the K valley: it is more pronounced for MoSe$_2$ and WSe$_2$ than for MoS$_2$ and WS$_2$ (cf. Figs. 7–11). In the case of MoTe$_2$, where mainly the valence bands at K are doped, a description with 2D, quadratic, isotropic bands completely fails.

For n-type doping of all TMDs the DOS at the Fermi energy shows a quasi-2D behavior. It has steps when the conduction-

band minimum at K or Q enters the bias window and is nearly constant in between. However, for larger electron doping the nonconstant behavior increases. This is due to the stronger deviation of the spin-orbit-split conduction band at Q from a quadratic dispersion.

The in-plane conductivity σ_{xx}/τ is another measure for the deviation from quadratic, isotropic bands in two dimensions. As can be seen in Eq. (16), for a perfect 2D electron gas the conductivity would be an increasing linear function of the doping-charge concentration n. Most interestingly, the right-hand panel of Fig. 18 shows that σ_{xx}/τ weakly differs from one TMD to the other and from the monolayer to the multilayer case. Only for the tungsten dichalcogenides the conductivity

has a small nonlinear component for n-type doping. This might be due to the stronger SOC of tungsten which leads also to larger deviation of the Q valley from a quadratic dispersion.

IV. CONCLUSIONS

In this work, we have calculated from *ab initio* the structural, electronic, and transport properties for monolayer, bilayer, and trilayer TMDs in field-effect configuration. We have first investigated the structural changes of the TMDs under field-effect doping. We found that the internal structure is only slightly changed but that it is nevertheless important to fully relax the system. We also showed that high electron doping can induce a phase transition from the 1H to the 1T$'$ structure. In accordance with literature this transition can, however, only occur for electron doping larger than n $\leqslant -0.35$ e/unit cell. Therefore, we concentrated on smaller doping of the H polytype as it is the most stable structure found in nature.

The band structure and thus also the transport properties can be changed considerably under field-effect doping. We have shown that most TMDs behave similarly under hole doping while for electron doping they can be divided into two different classes: one in which the conductive channel has a width of approximately two layers for small doping (MoSe$_2$ and MoTe$_2$) and one in which the charge is localized within the first layer. This can be attributed to the relative position of the conduction-band minimum at K and Q in the multilayer TMDs. In the former class Q is lower than K and the doping charge first occupies the states in the Q valley. Since these states have a large p_z contribution of chalcogen states, the hybridization between the layers is larger and the electrons are more delocalized. Additionally, for the tungsten dichalcogenides the difference between K and Q is smaller than for MoS$_2$ and thus, as the electron doping is increased, the charge rapidly starts to occupy states at Q. This leads to an increase of the width of the conductive channel to approximately two layers. For high electron doping only the Q valley is occupied in all investigated TMDs (also in the monolayer systems) and the width of the conductive channel is reduced to one layer.

Under hole doping most TMDs behave similarly: in the monolayer case first the valence-band maximum at K is occupied while in the multilayer case it is the Γ valley. This also leads to the delocalization of the doping charge over more layers as the states at Γ have large chalcogen p_z character. For large hole doping also in the monolayer case the doping at Γ is larger than those at K. The only exception from this picture is MoTe$_2$ in which the valence-band maximum for the undoped compound is always at K even in the multilayer case. Accordingly, the doping charge within the K valley is always larger than those at Γ.

However, even if the thickness of the doping-charge distribution is approximately two layers for multilayer TMDs, the number of doped valleys can be comparable to the monolayer case. The main difference is between n-type and p-type doping: as the valley degeneracy for the conduction-band minimum at Q is $g_v = 6$, the total number of doped valleys can be as large as $\nu = 16$ while for hole doping the maximum is $\nu = 8$.

In the next part, we have seen that a Hall-effect measurement can often not directly be used in order to determine the charge-carrier concentration under the assumption of quadratic bands—the charge thus determined can be up to 1.5 times larger than the real doping charge within the sample. For MoTe$_2$ the Hall coefficient R_{xyz} even changes the sign due to the changing curvature of the valence band. Thus, an interpretation based on parabolic bands would lead to an incorrect sign of the charge of the carriers. Even if this can only be seen at low temperatures, the Hall-effect measurement still largely overestimates the doping charge concentration if one does not take into account the specific band structure. Only in the case of multilayer MoS$_2$ the inverse Hall coefficient is directly proportional to the doping-charge concentration for a large range of electron and hole doping.

In this work, we have shown that it is important to correctly model an FET setup. The changes in the electronic and transport properties cannot be described with both the rigid doping and the uniform-background doping approach. We provide not only a full database of electronic structure of monolayer, bilayer, and trilayer dichalcogenides as a function of doping, but also a mapping between the doping charge and the Hall coefficient.

ACKNOWLEDGMENTS

[1] A. K. Geim and K. S. Novoselov, Nature Mater. **6**, 183 (2007).

[2] M. Z. Hasan and C. L. Kane, Rev. Mod. Phys. **82**, 3045 (2010).

[3] Q. H. Wang, K. Kalantar-Zadeh, A. Kis, J. N. Coleman, and M. S. Strano, Nature Nano. **7**, 699 (2012).

[4] G. Fiori, F. Bonaccorso, G. Iannaccone, T. Palacios, D. Neumaier, A. Seabaugh, S. K. Banerjee, and L. Colombo, Nature Nano. **9**, 768 (2014).

[5] R. Ganatra and Q. Zhang, ACS Nano **8**, 4074 (2014).

[6] D. Jariwala, V. K. Sangwan, L. J. Lauhon, T. J. Marks, and M. C. Hersam, ACS Nano **8**, 1102 (2014).

[7] X. Xu, W. Yao, D. Xiao, and T. F. Heinz, Nature Phys. **10**, 343 (2014).

[8] R. Könenkamp, Phys. Rev. B **38**, 3056 (1988).

[9] B. Radisavljevic, A. Radenovic, J. Brivio, V. Giacometti, and A. Kis, Nature Nano. **6**, 147 (2011).

[10] J. T. Ye, Y. J. Zhang, R. Akashi, M. S. Bahramy, R. Arita, and Y. Iwasa, Science **338**, 1193 (2012).

[11] S. Das, H.-Y. Chen, A. V. Penumatcha, and J. Appenzeller, Nano Lett. **13**, 100 (2013).

[12] S. Das and J. Appenzeller, Nano Lett. **13**, 3396 (2013).

[13] S. Najmaei, Z. Liu, W. Zhou, X. Zou, G. Shi, S. Lei, B. I. Yakobson, J.-C. Idrobo, P. M. Ajayan, and J. Lou, Nature Mater. **12**, 754 (2013).

[14] B. Radisavljevic and A. Kis, Nature Mater. **12**, 815 (2013).

[15] S. Wu, J. S. Ross, G.-B. Liu, G. Aivazian, A. Jones, Z. Fei, W. Zhu, D. Xiao, W. Yao, D. Cobden, and X. Xu, Nature Phys. **9**, 149 (2013).

[16] H. Yuan, M. S. Bahramy, K. Morimoto, S. Wu, K. Nomura, B.-J. Yang, H. Shimotani, R. Suzuki, M. Toh, C. Kloc, X. Xu, R. Arita, N. Nagaosa, and Y. Iwasa, Nature Phys. **9**, 563 (2013).

[17] H.-J. Chuang, X. Tan, N. J. Ghimire, M. M. Perera, B. Chamlagain, M. M.-C. Cheng, J. Yan, D. Mandrus, D. Tománek, and Z. Zhou, Nano Lett. **14**, 3594 (2014).

[18] C.-P. Lu, G. Li, J. Mao, L.-M. Wang, and E. Y. Andrei, Nano Lett. **14**, 4628 (2014).

[19] D. Ovchinnikov, A. Allain, Y.-S. Huang, D. Dumcenco, and A. Kis, ACS Nano **8**, 8174 (2014).

[20] M. Rösner, S. Haas, and T. O. Wehling, Phys. Rev. B **90**, 245105 (2014).

[21] N. F. Q. Yuan, K. F. Mak, and K. T. Law, Phys. Rev. Lett. **113**, 097001 (2014).

[22] K. F. Mak, K. L. McGill, J. Park, and P. L. McEuen, Science **344**, 1489 (2014).

[23] Y. Ge and A. Y. Liu, Phys. Rev. B **87**, 241408 (2013).

[24] T. Brumme, M. Calandra, and F. Mauri, Phys. Rev. B **89**, 245406 (2014).

[25] See Supplemental Material at http://link.aps.org/supplemental/10.1103/PhysRevB.91.155436 for the band structures of the undoped TMDs, a comparison between the band structure of relaxed and unrelaxed bilayer MoS_2 under field-effect doping, a comparison between the band structures of doped monolayer and trilayer $MoSe_2$ using either our approach of Ref. [24] or the uniform-background doping approach, a comparison between LDA and PBE for MoS_2, the band structures for all doping levels of the TMDs considered in this work, and a comparison between the inverse Hall coefficients calculated at $T = 0$ K and $T = 300$ K.

[26] P. Giannozzi, S. Baroni, N. Bonini, M. Calandra, R. Car, C. Cavazzoni, D. Ceresoli, G. L. Chiarotti, M. Cococcioni, I. Dabo, A. D. Corso, S. de Gironcoli, S. Fabris, G. Fratesi, R. Gebauer, U. Gerstmann, C. Gougoussis, A. Kokalj, M. Lazzeri, L. Martin-Samos, N. Marzari, F. Mauri, R. Mazzarello, S. Paolini, A. Pasquarello, L. Paulatto, C. Sbraccia, S. Scandolo, G. Sclauzero, A. P. Seitsonen, A. Smogunov, P. Umari, and R. M. Wentzcovitch, J. Phys. Condens. Matter **21**, 395502 (2009).

[27] P. E. Blöchl, Phys. Rev. B **50**, 17953 (1994).

[28] R. Roldán, J. A. Silva-Guillén, M. P. López-Sancho, F. Guinea, E. Cappelluti, and P. Ordejón, Ann. Phys. (Berlin) **526**, 347 (2014).

[29] J. P. Perdew, K. Burke, and M. Ernzerhof, Phys. Rev. Lett. **77**, 3865 (1996).

[30] S. Grimme, J. Comput. Chem. **27**, 1787 (2006).

[31] N. Podberezskaya, S. Magarill, N. Pervukhina, and S. Borisov, J. Struct. Chem. **42**, 654 (2001).

[32] H. J. Monkhorst and J. D. Pack, Phys. Rev. B **13**, 5188 (1976).

[33] M. Otani and O. Sugino, Phys. Rev. B **73**, 115407 (2006).

[34] O. Andreussi and N. Marzari, Phys. Rev. B **90**, 245101 (2014).

[35] O. Andreussi, I. Dabo, and N. Marzari, J. Chem. Phys. **136**, 064102 (2012).

[36] L. Bengtsson, Phys. Rev. B **59**, 12301 (1999).

[37] W. Shi, J. Ye, Y. Zhang, R. Suzuki, M. Yoshida, N. Inoue, Y. Saito, and Y. Iwasa, in *Bulletin of the APS* (APS, San Antonio, 2015), http://meetings.aps.org/link/BAPS.2015.MAR.J2.12

[38] Y. Lee, J. Lee, S. Kim, and H. S. Park, J. Phys. Chem. C **118**, 18278 (2014).

[39] N. R. Pradhan, D. Rhodes, Y. Xin, S. Memaran, L. Bhaskaran, M. Siddiq, S. Hill, P. M. Ajayan, and L. Balicas, ACS Nano **8**, 7923 (2014).

[40] N. R. Pradhan, D. Rhodes, S. Feng, Y. Xin, S. Memaran, B.-H. Moon, H. Terrones, M. Terrones, and L. Balicas, ACS Nano **8**, 5911 (2014).

[41] I. G. Lezama, A. Ubaldini, M. Longobardi, E. Giannini, C. Renner, A. B. Kuzmenko, and A. F. Morpurgo, 2D Mater. **1**, 021002 (2014).

[42] S. Jo, D. Costanzo, H. Berger, and A. F. Morpurgo, Nano Lett. **15**, 1197 (2015).

[43] D. Braga, I. Gutiérrez Lezama, H. Berger, and A. F. Morpurgo, Nano Lett. **12**, 5218 (2012).

[44] N. R. Pradhan, D. Rhodes, S. Memaran, J. M. Poumirol, D. Smirnov, S. Talapatra, S. Feng, N. Perea-Lopez, A. L. Elias, M. Terrones, P. M. Ajayan, and L. Balicas, Sci. Rep. **5**, 8979 (2015).

[45] G. Madsen and D. Singh, Comput. Phys. Commun. **175**, 67 (2006).

[46] H. Peelaers and C. G. Van de Walle, Phys. Rev. B **86**, 241401 (2012).

[47] W. S. Yun, S. W. Han, S. C. Hong, I. G. Kim, and J. D. Lee, Phys. Rev. B **85**, 033305 (2012).

[48] H. Shi, H. Pan, Y.-W. Zhang, and B. I. Yakobson, Phys. Rev. B **87**, 155304 (2013).

[49] D. M. Guzman and A. Strachan, J. Appl. Phys. **115**, 243701 (2014).

[50] E. Cappelluti, R. Roldán, J. A. Silva-Guillén, P. Ordejón, and F. Guinea, Phys. Rev. B **88**, 075409 (2013).

[51] A. Dal Corso and A. Mosca Conte, Phys. Rev. B **71**, 115106 (2005).

[52] K. F. Mak, C. Lee, J. Hone, J. Shan, and T. F. Heinz, Phys. Rev. Lett. **105**, 136805 (2010).

[53] A. Splendiani, L. Sun, Y. Zhang, T. Li, J. Kim, C.-Y. Chim, G. Galli, and F. Wang, Nano Lett. **10**, 1271 (2010).

[54] C. Ruppert, O. B. Aslan, and T. F. Heinz, Nano Lett. **14**, 6231 (2014).

[55] Y. Zhang, T.-R. Chang, B. Zhou, Y.-T. Cui, H. Yan, Z. Liu, F. Schmitt, J. Lee, R. Moore, Y. Chen, H. Lin, H.-T. Jeng, S.-K. Mo, Z. Hussain, A. Bansil, and Z.-X. Shen, Nature Nano. **9**, 111 (2014).

[56] J. K. Ellis, M. J. Lucero, and G. E. Scuseria, Appl. Phys. Lett. **99**, 261908 (2011).

[57] Q. Liu, L. Li, Y. Li, Z. Gao, Z. Chen, and J. Lu, J. Phys. Chem. C **116**, 21556 (2012).

[58] T. Cheiwchanchamnangij and W. R. L. Lambrecht, Phys. Rev. B **85**, 205302 (2012).

[59] Z. Y. Zhang, M. S. Si, Y. H. Wang, X. P. Gao, D. Sung, S. Hong, and J. He, J. Chem. Phys. **140**, 174707 (2014).

[60] L. Zhang and A. Zunger, Nano Lett. **15**, 949 (2015).

[61] A. Ramasubramaniam, D. Naveh, and E. Towe, Phys. Rev. B **84**, 205325 (2011).

[62] S. Bhattacharyya and A. K. Singh, Phys. Rev. B **86**, 075454 (2012).

[63] A. Kumar and P. Ahluwalia, Eur. Phys. J. B **85**, 186 (2012).

[64] L. Debbichi, O. Eriksson, and S. Lebègue, Phys. Rev. B **89**, 205311 (2014).

[65] T. Böker, R. Severin, A. Müller, C. Janowitz, R. Manzke, D. Voß, P. Krüger, A. Mazur, and J. Pollmann, Phys. Rev. B **64**, 235305 (2001).

[66] T. Fang, A. Konar, H. Xing, and D. Jena, Appl. Phys. Lett. **91**, 092109 (2007).

[67] J. Xia, F. Chen, J. Li, and N. Tao, Nature Nano. **4**, 505 (2009).

[68] K. Taniguchi, A. Matsumoto, H. Shimotani, and H. Takagi, Appl. Phys. Lett. **101**, 042603 (2012).

[69] Y. Zhang, J. Ye, Y. Matsuhashi, and Y. Iwasa, Nano Lett. **12**, 1136 (2012).

[70] S. Luryi, Appl. Phys. Lett. **52**, 501 (1988).

[71] D. L. John, L. C. Castro, and D. L. Pulfrey, J. Appl. Phys. **96**, 5180 (2004).

[72] N. Ma and D. Jena, 2D Mater. **2**, 015003 (2015).

[73] R. B. Somoano, V. Hadek, and A. Rembaum, J. Chem. Phys. **58**, 697 (1973).

[74] A. N. Enyashin and G. Seifert, Comp. Theor. Chem. **999**, 13 (2012).

[75] F. Wypych and R. Schollhorn, J. Chem. Soc. Chem. Commun., 1386 (1992).

[76] S. Jiménez Sandoval, D. Yang, R. F. Frindt, and J. C. Irwin, Phys. Rev. B **44**, 3955 (1991).

[77] G. Eda, T. Fujita, H. Yamaguchi, D. Voiry, M. Chen, and M. Chhowalla, ACS Nano **6**, 7311 (2012).

[78] M. Calandra, Phys. Rev. B **88**, 245428 (2013).

[79] M. Kan, J. Y. Wang, X. W. Li, S. H. Zhang, Y. W. Li, Y. Kawazoe, Q. Sun, and P. Jena, J. Phys. Chem. C **118**, 1515 (2014).

[80] S. L. Tang, R. V. Kasowski, and A. Suna, J. Vac. Sci. Technol. A **8**, 3484 (1990).

[81] A. Mar, S. Jobic, and J. A. Ibers, J. Am. Chem. Soc. **114**, 8963 (1992).

[82] A. Crossley, S. Myhra, and C. Sofield, Surf. Sci. **318**, 39 (1994).

[83] J. Augustin, V. Eyert, T. Böker, W. Frentrup, H. Dwelk, C. Janowitz, and R. Manzke, Phys. Rev. B **62**, 10812 (2000).

[84] G. S. Watson, B. P. Dinte, J. A. Blach, and S. Myhra, J. Phys. D: Appl. Phys. **35**, 2066 (2002).

[85] M. N. Ali, J. Xiong, S. Flynn, J. Tao, Q. D. Gibson, L. M. Schoop, T. Liang, N. Haldolaarachchige, M. Hirschberger, N. P. Ong, and R. J. Cava, Nature (London) **514**, 205 (2014).

[86] A. N. Enyashin, L. Yadgarov, L. Houben, I. Popov, M. Weidenbach, R. Tenne, M. Bar-Sadan, and G. Seifert, J. Phys. Chem. C **115**, 24586 (2011).

[87] Y.-C. Lin, D. O. Dumcenco, Y.-S. Huang, and K. Suenaga, Nature Nano. **9**, 391 (2014).

[88] Y. Kang, S. Najmaei, Z. Liu, Y. Bao, Y. Wang, X. Zhu, N. J. Halas, P. Nordlander, P. M. Ajayan, J. Lou, and Z. Fang, Adv. Mater. **26**, 6467 (2014).

[89] Y. Ge, W. Wan, W. Feng, D. Xiao, and Y. Yao, Phys. Rev. B **90**, 035414 (2014).

[90] M. Topsakal and S. Ciraci, Phys. Rev. B **85**, 045121 (2012).

[91] D. Lovett, *Tensor Properties of Crystals, Second Edition* (Taylor & Francis, Abingdon, 1999).